Universiteit Utrecht

Faculteit Bètawetenschappen
Faculteit Geowetenschappen

Modelling the response of a double-barred sandy beach system to time-varying wave angles

Bachelor Thesis

Mieka Driessen

Physics and Astronomy
Earth Sciences

Supervisors:

Prof. Dr. H.E. de Swart
Institute for Marine and Atmospheric Research (IMAU)

Dr. T.D. Price
Coastal Dynamics, Fluvial Systems and Global Change

Dr. A. Nnafie
Institute for Marine and Atmospheric Research (IMAU)

June 10, 2020

Abstract

On top of longshore-parallel bars, which often occur in sandy beach systems, 3D structures often form. Knowledge about the dynamics of barred sandy beach systems can be used for the preservation of coast and decrease the number of incidents in the nearshore area due to currents. Different model studies have investigated the response to different constant wave forcing (change in angle of incidence, wave height and wave period) as well as the stability of a double-barred beach system. A study on the influence of time-varying wave angles on a double-barred beach system is still missing. This study aims to find the response of a double-barred beach system to sinusoidally time-varying wave angles at the offshore boundary, for a mean wave angle normal to the coast and for non-zero mean wave angles. The non-linear model Morfo55, which solves the coupling between currents, wave, sediment transport and bottom evolution, is used to study the morphological evolution of the double-barred system. The angle of incidence at the offshore boundary is sinusoidally varied for different periods and amplitudes, including a reference case in which the period was set to 0 days (constant wave forcing). Simulations were done for both the case with a mean normal wave angle and a non-zero mean wave angle, leading to a better understanding of a double-barred system.

The reference cases, with constant wave conditions, show bar growth on the inner and outer bar for a mean normal angle. For the case with an oblique mean angle, there was no bar growth on the outer bar, only on the inner bar. Both reference cases have a larger mean bar growth in the inner domain than for time-varying wave angles. In the outer domain, the bar growth is approximately the same for time-varying angles and for constant angles, provided that bars form.

The root-mean square bar height, $||h||$ showed oscillating behaviour with a response period, $T_{||h||}$, and a standard deviation with respect to the mean bar height, $\sigma_{||h||}$. An increase in period of the time-varying waves resulted in an increase of the response period $T_{||h||}$ as $T_{||h||} = \frac{1}{2}T_\theta$ for cases with a normal mean angle in both the inner and outer domain. The standard deviation increase for increasing T_θ with a peak for $T_\theta = 15$ days. For the cases with an oblique mean angle, two dominant response periods were found in the inner domain, $T_{||h||} = \frac{1}{2}T_\theta$,$T_\theta$, and one in the outer domain, $T_{||h||} = T_\theta$. In these cases $\sigma_{||h||}$ increases for an increase in T_θ.

An increase in the amplitude of the angles, A_θ, resulted in a decrease in the mean bar growth and an increase in the response time, $t_{||h||}$ of the outer bars. The response time of the inner bars did not change. Both results were enhanced by an oblique mean wave angle instead of a normal mean wave angle.

Front page: Double wave breaking in the nearshore area of a sandy beach in the Gold Coast, Australia (https://www.mynrma.com.au). The breaking of waves a few tens of meters from the coastline shows an interrupted pattern in the longshore direction.

Contents

1 Introduction

1.1 General setting and relevance

Beaches and water play a key role in life on earth. They are a source of life and food and have ecological and economical value. Water acts as a natural barrier used for protection against nature and humans, but also as a means to transport people and cargo over large distances. Especially in our current economic system, water also plays a large role in providing energy. Most of the Earth's water, 96.5%, is contained in seas and oceans (Gleick 1993). Therefore, it is no wonder that half of the population lives in close proximity, less than 100 km, to the coast (Davis Jr. and Fitzgerald 2004). Even though only 0.05% of the landmass surface consists of coastal zone, the 440,000 km of coastline is a considerable amount. These 440,000 km comprise a wide variety of different coastal forms. Some examples are swamp deltas, estuaries, coral reefs, rocky coasts, fjords and sand beaches (Marshak 1955). Recent observational studies have shown that, with the exception of icy coast, 31% of the total coastline consists of sandy beaches (Luijendijk et al. 2018). It are these beaches that will be considered in this thesis. Sandy beaches are a natural barrier between storm waves and the populated coastal area. They also have the ability to adapt to changes in the sea level. Due to many forms of erosion, sandy beaches are constantly changing. These coastal areas can be dangerous places and pose a danger for swimmers and sailors. Research has shown that the deaths by very strong currents in the coastal area cause more deaths on a yearly basis, 21 fatalities, than bush fires, floods, and cyclones together (Brander et al. 2013). The reported fatalities in the USA lie at 35 on average each year (Gensini and Ashley 2010).As such, it is necessary to obtain a deeper understanding of sandy beaches and their respective dangers in order to accurately inform both visitors and residents of the coastal area.

The coastal area can be divided in different zones, based on either morphological features or wave conditions (see Figure 1). Based on morphology, the backshore is the landward boundary of the coastal zone. It consists of only sediment and sometimes some vegetation. Sea water never reaches this part under normal conditions. The second zone is called the foreshore zone or intertidal zone. This is the part of the beach between the coastline at low and high tide. The nearshore zone, also called littoral zone, is the area starting at the foreshore zone and ending at the point where bottom sediment transport ceases. The offshore zone starts where the nearshore zone ends. At this point, the bottom of the sea is no longer influenced by waves (Marshak 1955). This depth can vary between the 10 and 30 meters depending on the wave conditions (A. Short and Woodroffe 2009).

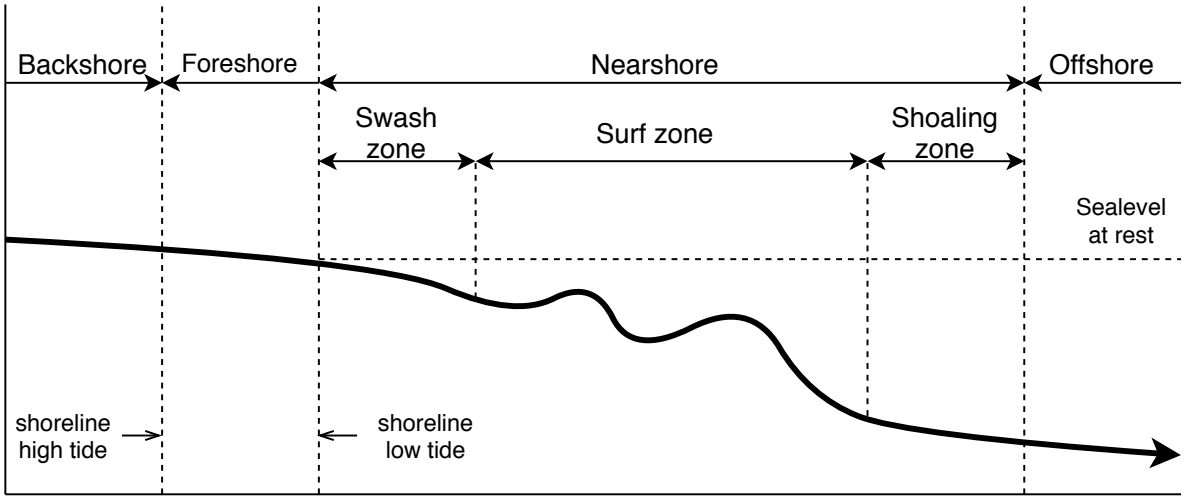

Figure 1: A sketch of a beach profile with the different zones. The bottom is indicated with the solid thick black line. The division of different zones is indicated with vertical dashed lines. Based on Haslett 2000

Different wave conditions give the possibility to subdivide the nearshore region in a swash zone, a surfer zone or breaker zone and the shoaling zone. When waves move in the direction of a coast, their height, wavelength and angle of direction change due to variations in depth. The influence of the depth becomes substantial when the water depth is approximately 0.5 of the wavelength of the waves, called the wave base (Groen and Dorrestein 1976, Marshak 1955). At a lower depth, the wave movement of the water parcels is less than 4% of that of the water at the surface. At the point where the wave base touches the bottom of the sea, the shoaling zone begins. The zone where waves start to break is called the breaker zone or surf zone. After breaking, a surge of water is sent onto the beach in the swash zone. This thesis focusses on the littoral zone, in particular the surf zone.

Observations have shown that a recurring morphological phenomenon in the surf zone of sandy beach areas are sand bars in the near-shore region. These sandbars can be divided into two categories based on the beaches where they are formed. Beaches with tidal ranges are referred to as ridge and runnel beaches and non-tidal beaches are called barred beaches (King and Williams 2020). The latter is of interest in this thesis. When we know how sandbars work, we might be able to prevent or reduce erosion more effectively, as has been done by the Dutch government in cooperation with scientist, in the form of shore face nourishment by a sand engine (Stive et al. 2013).

Barred beaches display two distinct bar patterns (Wright and A. D. Short 1984). The first are shore-parallel, uniform, straight sandbars as presented in the upper panel of Figure 4, from now on referred to as uniform bars. These uniform, parallel bars can form with more than one at a time, but rarely exceed four. The second bar patterns are called crescentic bars, presented in Figure 2 and the lower panel of Figure 4, hereafter referred to as bars. Crescentic bars show a periodically alternating deeper part, bays or troughs formed by rip channels and shallow parts, the horns or shoals. An example of a crescentic bar be seen in Figure 2, where the darker colours indicate the deeper parts. The distance between the horns and bays is often regular in the longshore direction (Price et al. 2014). However, this does not have to be the case. The horns and bays can change position and by doing so, a bay/horn can disappear and two horns/bays can become one, this process is called merging. This process can also occur in reverse, one horn/bay can split in two smaller horns/bays,

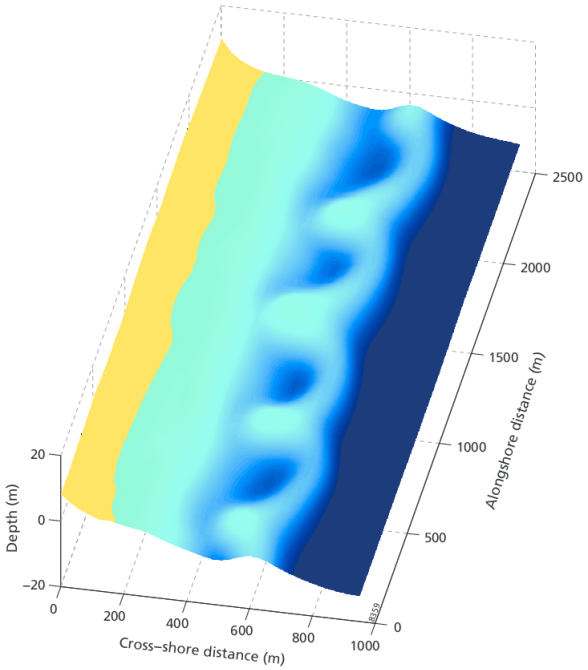

Figure 2: A crescentic sandbar with an undulating pattern of deeper bays and shallow horns, based on data from Almar et al. (2010), figure made by Price et al. (2014). The darker the colour, the deeper the area. The light blue area are the shallow parts and the yellow part represents the sandy beach.

this process is called splitting of bars. The main interest of this study is the response of a double-barred system to different wave conditions.

When waves arrive at the coast, they push the water up onto the beach, causing the water level to rise. A net sediment transport in the direction of the coast is part of this process. When the component perpendicular to the coast can not proceed any further up the beach, it flows back to the sea in a flow perpendicular to the coast, undertow, during storm conditions or it flows side ways under normal conditions. When two currents parallel to the coast collide, they form one current that flows back to the sea. The retreating water will take the path of least effort. When there are small differences in the depth, a longshore pressure gradient exists from shallow areas to deeper parts. The seaward transport of water happens in currents in these deeper areas. These are called rip currents and cause rip channels (i.e. the bays in the crescentic bars) to form. The sediment transported by the rip currents is deposited in seaward direction at so called rip heads. The beach system of the crescentic bars is often referred to as rip channel systems (Ribas et al. 2015). These rip currents can pose a danger to swimmers (Marshak 1955).

The transport of sediment and the characteristics of of currents in a barred beach system depend on the wave conditions (wave height, angle of incidence, period) and morphological conditions (bar heights, position of bars). For higher waves, the wavebase reaches larger depths and can thus cause more sediment to be transported. The angle of incidence has an influence on the strength of the different currents that develop. When bars lie deeper, the influence of wave breaking over these bars is smaller and sediment transport is less than for higher bars. So the wave height and depth of the bars have a similar effect on the system.

When the waves enter the coastal area, their wavevectors do not have to be normal to the coast. The wavevectord often have an angle with respect to a line normal to the coast. This angle decreases due to a process called refraction. The part of the wavcecrest closest to the coast starts to feel the influence of the bottom first and this part of the wave slows down. The part of the wave further away from the coast continues with its initial speed until this part also starts to slow down due to an elevation of the bottom. As a result, the wavevector becomes curved. This process does not totally diminish the angle, thus the wavevector has a component normal to the coast and one parallel to the coast (Haslett 2000). The component of the waves parallel to the coastline result in a current parallel to the coast, called longshore current. This current is able to transport sediment in the longshore direction, the longshore drift. This process can be seen in Figure 3.

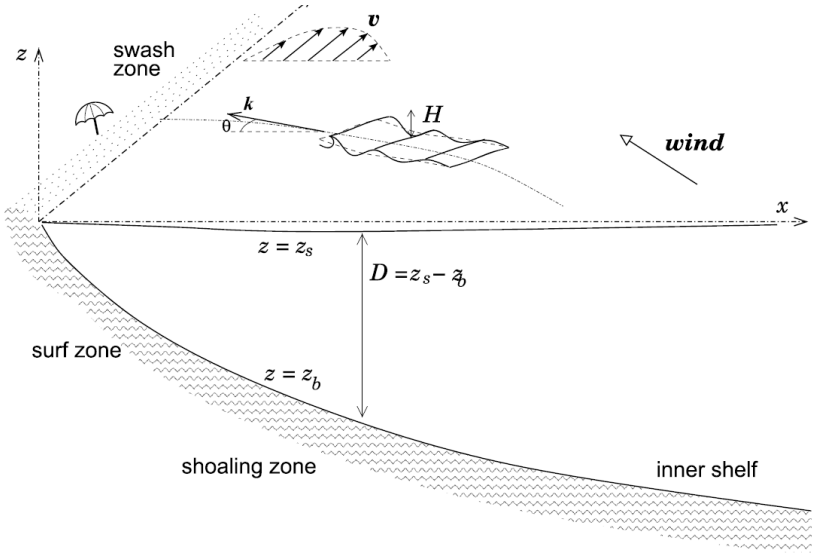

Figure 3: The effect of refraction is presented (the curved wavevector $\boldsymbol{k}$). The net current in the longshore direction is given by the arrows parallel to the coast with a velocity $\boldsymbol{v}$ (Ribas et al. 2015).

1.2 Previous research

Different kinds of research have already been done on the subject of barred beaches system. They can be divided in groups based on their approach of which two are discussed in this section. Some articles are based on long-term observations of different coasts, while others focus on non-linear numerical models.

1.2.1 Observations

Observations done by Lippmann and Holman (1990) show that crescentic bar patterns vanish during storm conditions when the wave energy is high, leaving only the shore-parallel uniform bars. When the storm ceases, this configuration turns out to be unstable. After about two days, crescentic bar patterns start to form again on top of the existing shore-parallel uniform bars. This takes them typically 5-16 days. These crescentic bars are tend to become stable stable under moderate wave conditions. Figure 4 shows the two states for high energy conditions and low energy conditions in the upper and lower panel respectively. The red lines are plotted over the lighter areas in the figure, indicating the shallow parts of the coastal area. The two figurations in this figure can merge from one two another, depending on the wave conditions.

The crescentic bars are constantly changing in both space and time, even when the characteristics of the incoming waves (height, period, angle of incidence) are almost constant. Van Enckevort et al. (2004) analysed long-term observation of single-barred beach systems at different sites. The researchers found variations in the wavelength and amplitude of crescentic bars in both space and time. The largest spatial difference in the wavelength between the largest and smallest crescentic bar was approximately a factor 2. The temporal

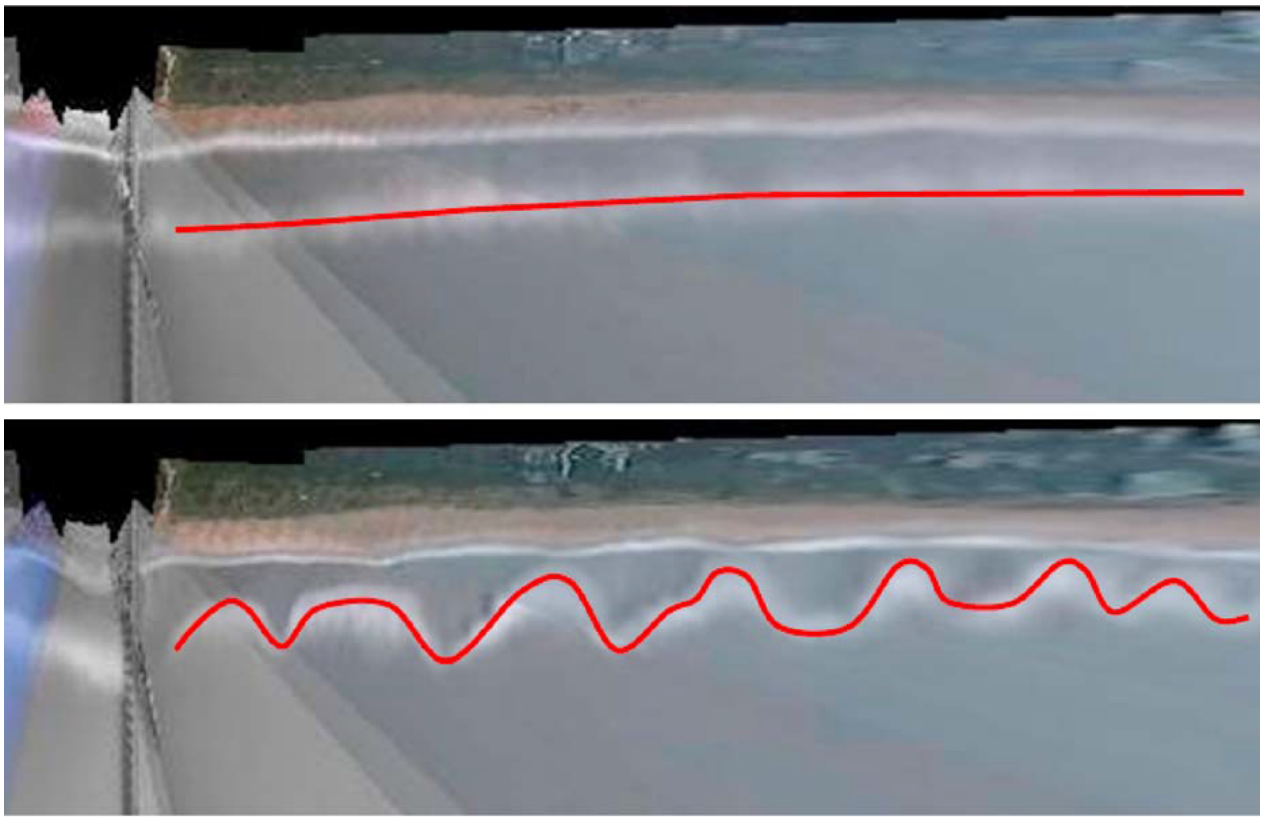

Figure 4: Time exposure of video images during 10 minutes of the coastal area (Duck, North Carolina, USA). The breaking of waves happens above shallow areas, indicated by the white of the foam of breaking waves. The red lines indicate the breaker lines. The two panels show the configuration of the beach system at different moments in time. A straight longshore parallel uniform bar configuration is presented in the upper panel of the figure. The lower panel shows a crescentic bar pattern. Figure from Garnier et al. (2013)

differences of the bars are caused by the system to become uniform in the longshore direction by splitting of the largest bars and merging of the smallest.

A study of a double-barred system done by Castelle et al. (2007) shows that the growth of bars in the outer domain is strongly coupled to the significant wave height H_s at the offshore boundary. The bars in the outer domain remained inactive for $H_s < 3$ m. Ruessink et al. (2007) observed the response of a double-barred beach system in the Gold Coast (Australia). Their observations show that the three dimensional patterns on top of the uniform shore-parallel bars vanish during storm conditions, which is similar to what was found by Lippmann and Holman (1990). After the storm event, the inner and outer bars were uncoupled. However, after some time, three-dimensional bars formed in the areas of both the inner bar and outer bar. These patterns were coupled, i.e. the growth of the bars in the inner domain are influenced by the growth of the bars in the outer domain.

A model to describe the development of different types of coupling between the inner and outer bars, based on observations, has been proposed by Price et al. (2014). This model is based on the relative position of the horns and bays on the inner and outer bar, the energy of the waves and the 3D structure of the inner bar (see Figure 5. When the horns and bays on the inner and outer bar are situated at the same longshore location, than the bars are in-phase (I). When the alongshore location of the horns (bays) on the inner bar coincides with the location of the bays (horns) on the outer bar, than the bars are out-of-phase (O). Low energy conditions are called downstate (d) and high energy conditions are called upstate (u). The inner bar displayed two different configurations, one where the inner bar was a shore-attached terrace (t) and one where rip channels occurred (r). For the low energy wave conditions (downstate), 4 different coupling types were found, so all combination of the in-phase out-of-phase and terraced or channelled configurations were found. For the high energy wave conditions, only one coupling was found, an out-of-phase terraced coupling. For oblique waves the bar growth was lower and for large angles ($\theta > 30^o$) the bars straightened and no alongshore variability in depth was found on the inner bar

1.2.2 Models

In addition to the research that focused on analysis and interpretation of observations, models have been developed to simulate a barred beach system. Most of this research focussed on a single-barred beach system. Single-barred beach systems tend to become stable in space and time under constant wave forcing. A stability analysis for waves with a normal and oblique incidence was done by Garnier et al. (2006). The researchers found that gravitational down-slope sediment transport is the driving force behind the stop in growth of the amplitudes of the bar.

The response of a single-barred system to different significant wave height, H_s, and period, T, has been modelled by Castelle and Ruessink (2011). They first performed simulations with different time-invariant wave height, H_s, period, T, and wave angle at the offshore boundary, θ_0 for mean wave incidence both normal to the coast and non-normal to the coast. For larger H_s and T, the growth rate of the bar increased. In increase in the angle θ_0 resulted in an increase in the alongshore spacing between bars. Next, they considered time-variable H_s and T and a zero mean angle of incidence, the same observations were done. For large H_s and T, the growth rate was higher. The overall growth rate decreased with an increase of the amplitude with which the wave height and period changed. The distance in the longshore direction between two sequential bars are the same for different amplitudes. When they considered periodically varying angles of wave incidence with a mean normal incidence, they observed crescentic pattern and splitting and merging of bars for low amplitudes. For larger amplitudes in the variation of the angle ($A_\theta = 6^o$), crescentic bars still formed, but no merging or splitting took place. When increasing the amplitude even further ($A_\theta = 8^o$) the bars straightened and no crescentic patterns formed on the uniform bar.

A similar study has been done by Rutten et al. (2019) for a curved coast, in contrast to the previously mentioned studies. Rutten et al. (2019) considered both time invariant and time-varying angles and the influence of the curvature of the coast on the formation of patterns on the uniform bar. The growth rate appeared

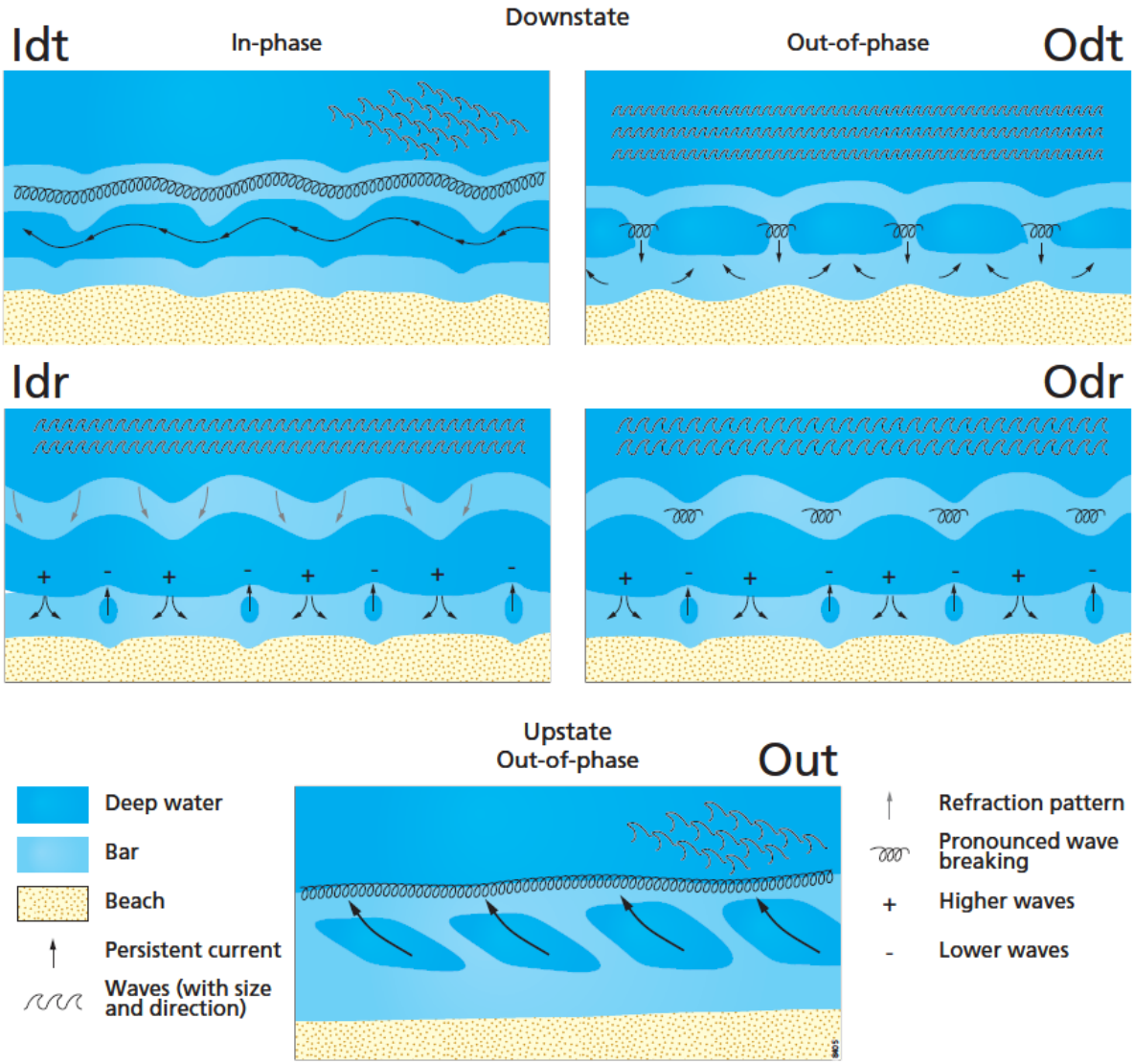

Figure 5: A model for different coupling types, based on observations. The coupling types have been named based on some characteristics: In-phase or out-of-phase (I or O), downstate or upstate (d or u), terraced or with rips (t or r). The longshore direction is given on the horizontal axis and the cross-shore direction on the vertical axis. Figure from Price et al. (2014)

to be largest for near-normal angles. An increase in the curvature of the coast can lead to an increase of near-normal angles and will thus cause an increase in the formation of patterns on the uniform bars.

This research was complemented by Nnafie et al. (2020). They investigated the influence of periodically time-varying wave angle incidence normal to the coast as well an oblique mean angle. For waves with varying wave angle, θ^0, and mean angle, $\theta_0^0 = 0^o$, the mean bar height could become larger than for waves with a constant angle $\theta^0 = 0^o$, depending on the forcing period T_θ and amplitude A_theta that was imposed on the wave angle. In the cases with an oblique mean angle, the mean bar height was smaller for time-varying wave angles than for constant wave angles. Especially when the amplitude of the variations increased, the growth rate decreased. In this study they also compared the mean bar height for different time-invariant wave angles. This showed that the largest growth of the root-mean square bar height was largest for $\theta^0 = 1.5^o$, 3^o. When the bars became larger than approximately 8^o, no bars formed.

Double-barred beach systems have also been studied with numerical models using different kinds of analysis. A stability analysis has been done by Klein and Schuttelaars (2006) and Coco et al. (2020). Klein and Schuttelaars (2006) focussed on the influence of the initial bed conditions for waves with an oblique angle of incidence. They found that there was no equilibrium in the bar height $||h||$. Coco et al. (2020) analysed the stability of the morphodynamics of a double-barred beach system for different offshore wave heights and depth of the bars. The outer bars did not grow for large differences in the depth of the inner and outer uniform bar or small wave heights, only the inner bars developed. For large wave heights or small differences between the depth of the two uniform bars, the outer bars fully developed. The activity on the outer bar dominated. For intermediate depth differences and wave conditions, both bars fully developed.

Smit et al. (2008), showed simulations of a double-barred beach system for constant wave conditions. The irregular patterns on the inner bar were smaller than the ones on the outer bar. Another result was that the response of the bar system depended on the volume of the bar. An increase in the bar volume results in an increase in response time. In most simulations, the outer bar has a larger height the inner bar and therefore also a larger volume.

The coupling between the inner bar and the outer bar has been modelled and studied by Castelle et al. (2010), with the use of Morphodyn, a non-linear time- and depth-averaged model, coupled with the spectral wave model SWAN (Castelle et al. 2006). They modelled three coupling types, in-phase, out-phase and at half of the outer-bar wavelength (see Figure 6). The first is a configuration where the horns on the inner bar face horns on th eouter bar, as can be seen from panel a) in Figure 6. Coupling of the bars at half the wavelength of the outer bars is presented in the middle panel, b) of this figure. The out-of-phase coupling is presented in panel c) of Figure 6, here bays on the inner barface the horns on the outer bar. The in-phase coupling was predominantly found for weakly developed outer bars and low energy wave. The out-of-phase coupling was found for well-developed outer bars and high energy waves. The coupling at half the wavelength of the outer bar was found in the more intermediate wave conditions.

Price et al. (2013) studied the coupling of the inner and outer bar as well, for constant, oblique wave of incidence with the same model as Castelle et al. (2010). For relatively small angles ($\theta < 10^o$), a coupling took place between the outer and inner bar. Where the outer bar had moved landwards, a horn in the undulating pattern called a rip bay occurred in the inner bar, as shown in Figure 7. For large angles, the bars were not coupled. In contrast to other double barred beach studies, Price et al. (2013) derived their bed profile and wave conditions from video observations at the Gold Coast.

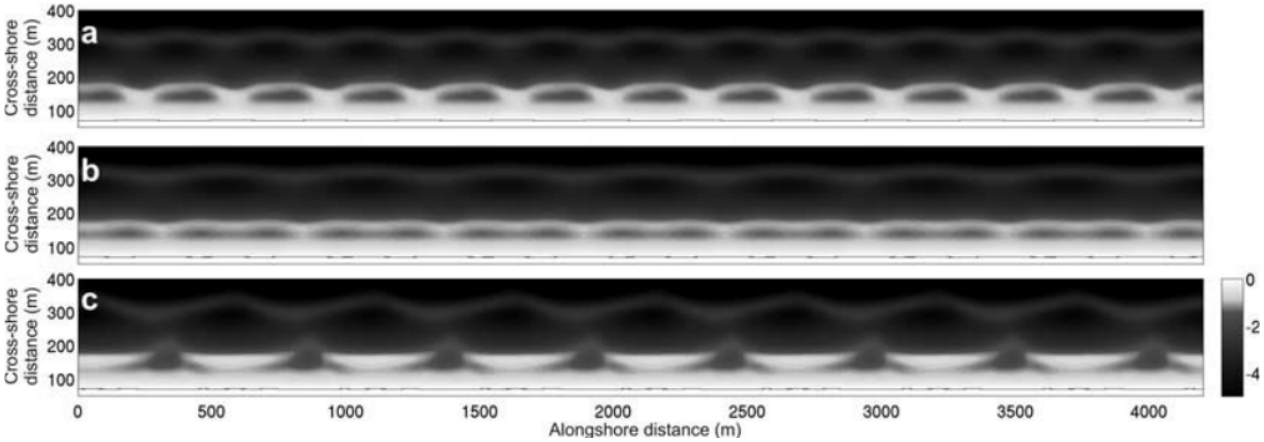

Figure 6: The coupling between the inner and outer bars as found by a study of Castelle et al. (2010) are presented for a) in-phase coupling b) coupling t half the wavelength of the outer bar c) out-of-phase coupling. Lighter areas indicate the shallow regions, darker areas indicate deep parts of the system.

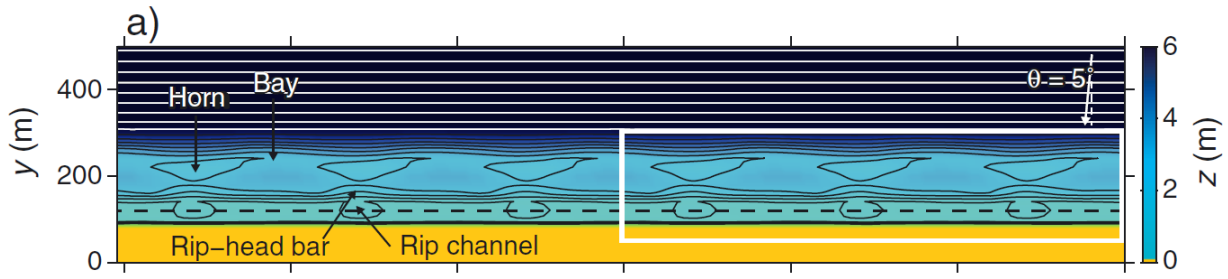

Figure 7: One of the results obtained by Price et al. (2013) showing the bathymetry of a simulation with a constant angle of incidence $\theta^0 = 5^o$. The lighter colours show shallow areas and the darker colours are deeper parts. The black lines are areas with the same elevation.

A non-linear model based on the depth-average shallow water equations, Morfo55, was used by Thiebot et al. (2012). The difference of this model compared to the one used by Castelle et al. (2010) and Price et al. (2013) is a difference in wave model and the formulation of the sediment transport. Thiebot et al. (2012) studied the effects of different constant wave angles on the formation of crescentic patterns on the inner and outer bar. For small wave angles ($0^o < \theta < 11^o$) crescentic patterns occurred. Coupling between the outer and inner bar is another result of their study. They found that when the outer bar started to form three-dimensional patterns first, the patterns on the inner bar would be coupled to the outer bar pattens. It did not work the other way around. The patterns on the outer bar were not influenced by the ones on the inner bar.

So far, the influence of the wave height, the difference in depth, the volume of the bars and the angle of incidence for a double-barred sandy beach system have been studied. This has been done by choosing different input parameters, while keeping the wave forcing constant. But none of the research on double-barred systems have focussed on the effects of time-varying wave angles as has already been done for single-barred systems (Castelle and Ruessink 2011; Nnafie et al. 2020). Observations show that wave conditions constantly change, so to get a better understanding of the real situations, the influence on time-varying wave forcing needs to be investigated. This study focusses in particular on the double-barred beach systems and how different, periodically varying wave conditions cause different patterns to form.

1.3 Research aims

The topic of the influence of time-varying wave conditions on a double-barred system has not been completed. Although previous research showed the response of barred beach systems to constant wave forcing (period, wave height and angle of incidence), the response to time-varying wave forcing has only been studied for single-barred beach systems. The response of a double-barred system to wave angles that vary periodically in time on the offshore boundary is missing. The main question of this study is: *What is the response of a double-barred beach system to periodically time-varying wave angles?* This will be answered based on 3 sub-questions: *What is the influence of the forcing period of the angles?; What is the influence of the maximum amplitude of the variations in the angle?; What is the influence of the mean angle?*. The hypothesis was that crescentic bar patterns would form, either on the inner uniform bar, or on the outer uniform bar, or both, depending on the wave height and angle. When patterns form on both uniform bars, the alongshore variability in the depth of the inner bar would likely be smaller than the ones on the outer bar. Furthermore, the patterns of the inner bar were expected to develop before patterns on the outer bar (Smit et al. 2008). There was also a possibility of a coupling between the patterns on both bars as in the studies by Castelle et al. (2010), Price et al. (2013), and Price et al. (2014). The largest mean bar height was expected for small angles (see Castelle and Ruessink (2011))

To answer this question, a non-linear model, Morfo55 was used. This model simulates the coupling between the wave dynamics, currents sediment transport and bed evolution. A detailed description of this model is given in Section 2. In Section 3, the method used for this experiment and the simulations that are done is explained. The results are presented in Section 4 and they are discussed and compared to previous research in Section 5. A discussion about the model is also be given in this section as well as some possibilities for further studies. Finally, the conclusions of this study are provided in Section 6.

2 Model

The non-linear model Morfo55 was used to study the evolution of the double-barred beach system. This model was first introduced by Caballeria et al. (2002) as Morfo50. Morfo55 is an improved version presented by Garnier et al. (2006). It is a non-linear numerical model which solves the depth-averaged shallow water equations and by doing so, it couples currents, waves, sediment transport and bed evolution.

2.1 Domain

Morfo55 employs a Cartesian coordinate system with the origin O at the coast, with the x-axis in the cross-shore direction and the y-axis in the longshore direction. The domain is a rectangle, confined by the lines $x = 0$, $y = 0$, $x = L_x$ and $y = L_y$. The chosen length of the domain in the longshore direction must be large enough, to ensure that the boundaries have no influence on the results. The z-axis is upwards, perpendicular to the xy-plane with $z = 0$ the initial sea level with no waves. The angle of incidence, θ^0, at the offshore boundary, $x = L_x$, is the angle between the wave vector $\boldsymbol{k}$ and the negative x-axis. Thus $\theta^0 = 0$ is defined perpendicular to the coast and a positive angle means a wave with a component in the positive y direction. A sketch of the domain is illustrated in Figure 8 (Garnier et al. 2006).

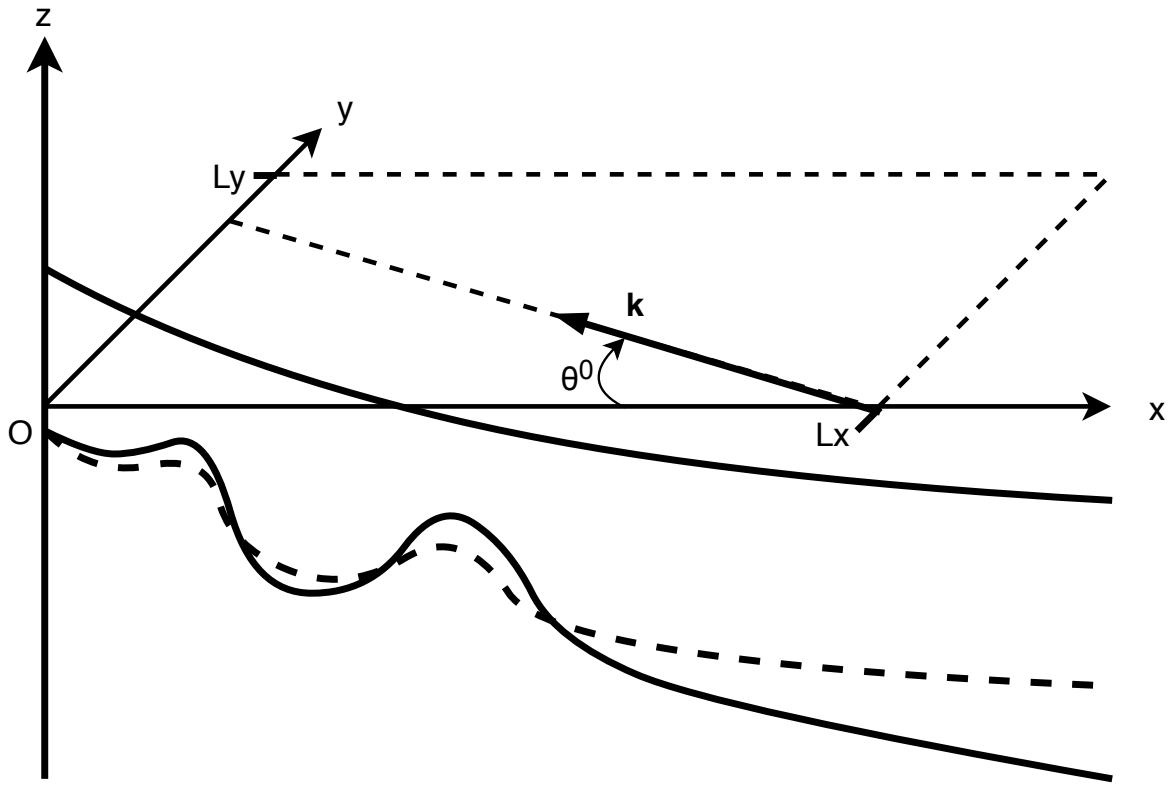

Figure 8: A schematic view of the domain used for Morfo55. The domain modelled in a Cartesian coordinate frame with x the cross-shore direction, y the longshore direction and z perpendicular to y and x, pointing upward. The domain is bounded by the boundaries $x = 0$, $x = L_x$, $y = 0$ and $y = L_y$. The dashed line is the time and longshore averaged bed level, the current bed level is shown as the unperturbed line close to the dashed line. Furthermore, θ^0 is the angle of incidence of the waves at the offshore boundary with respect to shore-normal.

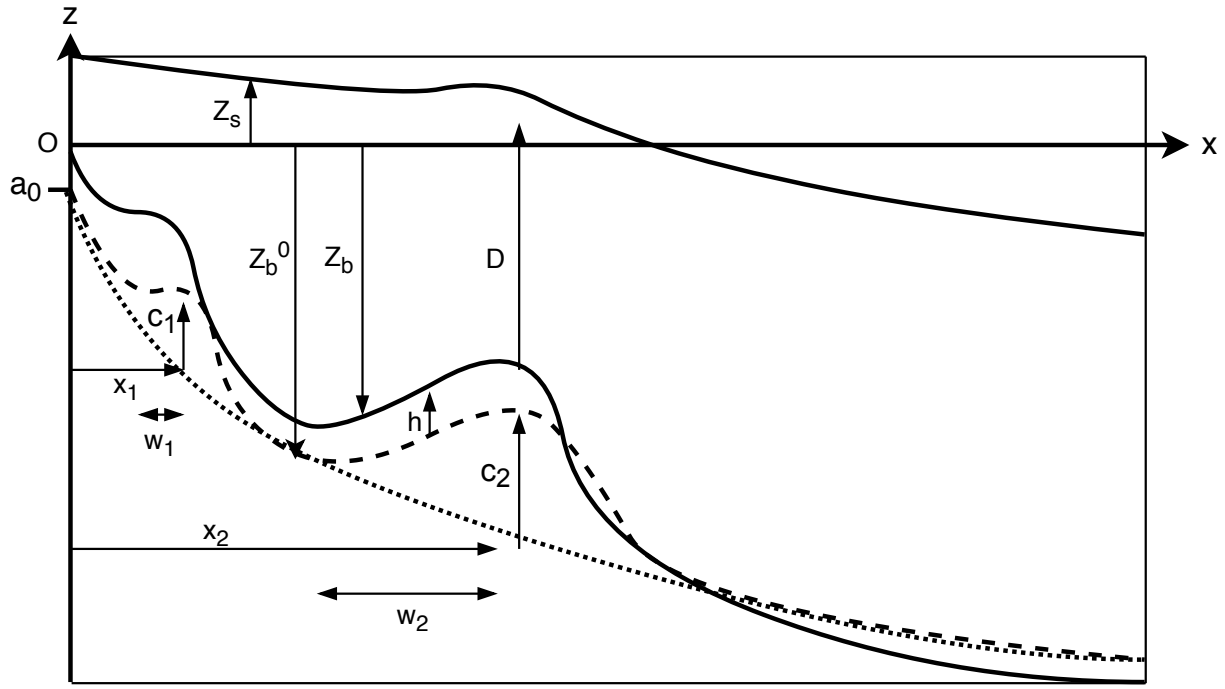

Figure 9: A sketch of the profile used for the simulations. The mean water level is $z = 0$ and z_s is the actual water level. The dotted line illustrates the smooth bed level without any bars, the dashed line indicates the averaged profile with two bars and the slightly different full line denotes the actual bed level.

2.2 Bed-profile

The Morfo55 model was used by Garnier et al. (2006) for a beach system with a single bar. For this research, the profile of the bed level, z_b, given by Yu and Slinn (2003) was extended to a double-barred beach system. The modified model reads,

$$z_b^0 = -a_0 - a_1 \left(1 - \frac{\beta_2}{\beta_1}\right) \tanh\left(\frac{\beta_1}{a_1} x\right) - \beta_2 x + c_1 e^{-\left(\frac{x-x_1}{w_1}\right)^2} + c_2 e^{-\left(\frac{x-x_2}{w_2}\right)^2}. \tag{2.1}$$

Here, a_0 is the depth at the coastal boundary, a_1 is the form of the decay in the slope, β_1 is the dominating slope of the part nearshore part of the profile and β_2 the slope of the seaward part of the beach profile. The amplitudes of uniform, shore-parallel inner and outer bars are labelled as c_1 and c_2 respectively. Furthermore, w_1 and w_2 denote the width of the bars and the positions with respect to the y-axis is represented by x_1 and x_2.

The bed level, z_b^0, is not dependent of t and y, it is a time- and longshore averaged beach profile. A sketch of this profile with some other variables are shown in Figure 9. In this figure, the smooth profile without any bars is illustrated via the dotted line, the averaged profile with a double bar is illustrated via the dashed line and the actual bottom level is illustrated as the full line. The mean sea-level for is $z = 0$, whereas $z = z_s$ is the actual (wave-averaged) or dynamic water level. As mentioned before, z_b^0 is the averaged bed level over time and along the y-axis with respect to the mean sea level $z = 0$, z_b is the actual bed level with respect to $z = 0$. When referring to the uniform, shore parallel bars, the bottom profile of $z = z_b$ is meant. The total mean depth is defined as $D = z_s - z_b$ and is thus positive as long as $z_b < z_s$. The difference between the actual and the averaged bed level is defined as $h = z_b - z_b^0$(Garnier et al. 2006). As such, h is the perturbation on top of the uniform bars.

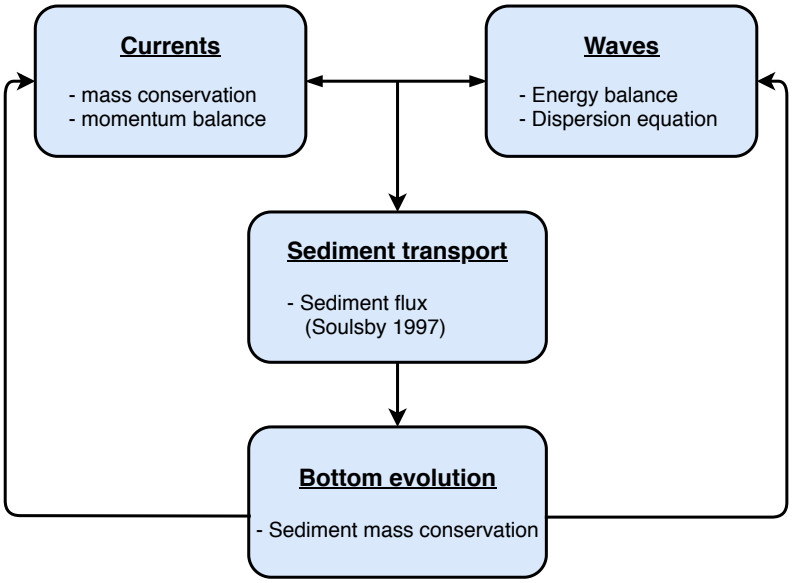

Figure 10: A flow diagram of the model Morfo55 showing the coupling between the different equations.

2.3 Governing equations

The hydrodynamics of the Morfo55 model is divided into a part which describes the currents of the system and a part involving the waves. The hydrodynamics of the system are coupled to the sediment transport and the bottom evolution with sediment equations. The model solves this set of equations and uses previous output as the input for a new time-step. A flow diagram of the model is provided in Figure 10.

2.3.1 Waves

The waves are incorporated in the system by the wave energy density balance equation, which reads

$$\frac{\partial E}{\partial t} + \frac{\partial}{\partial x_j}\left(\left(v_j + c_{gj}\right) E\right) + S'_{ij}\frac{\partial v_j}{\partial x_i} = -\varepsilon. \qquad i = (1,2) \tag{2.2}$$

This equation was incorporated in the Morfo55 model by Garnier et al. (2006) and is one of the improvements made on the Morfo50 model. Einstein's summation convention is used i.e. repeated indices in a term mean a summation over all its values. For generalisation, the formulas are given with indices $i = (1,2)$ in this case $(x_1, x_2) = (x, y)$ and (v_1, v_2) are the currents in the cross-shore and longshore direction respectively. Furthermore, $\boldsymbol{v}$ is the depth-averaged current vector $(v_1, v2)$, $E(x_1, x_2, t)$ is the energy density of the waves and is related to $H_{rms}(x_1, x_2, t)$, the root-mean square wave height, as follows: $E = \rho g H_{rms}^2/8$. The components of the group velocity of the waves are denoted by c_{gj}, S'_{ij} are the components of the stress tensor $\boldsymbol{S'}$. The wave energy density dissipation rate ε is a combination of the bottom friction and wave breaking: $\varepsilon = \varepsilon_f + \varepsilon_b$. The former is been described by Horikawa (1988) and the latter one by Thornton and Guza (1983). The wave energy can be coupled to the wavenumber k with the use of the intrinsic frequency σ i.e. the frequency of the current waves. The wave frequency $\omega = \sigma + v_j k_j = 2\pi/T$ is constant because the wave period T is set at the offshore boundary. Because $v_j k_j << \sigma$ it follows that $\sigma = 2\pi/T =$ constant. From linear wave theory, the dispersion relation for gravity waves states:

$$\sigma^2 = gk \tanh(kD). \tag{2.3}$$

Here, $D(x_1, x_2, t) = z_s - z_b$, the total mean depth (see Section 2.2) and g is the gravitational acceleration (9.8 m s^{-2}).

The frequency is related to the phase and group velocity by $c = \frac{\sigma}{k}$ and $c_g = \frac{\partial \sigma}{\partial k}$, yielding

$$c = \sqrt{\frac{g}{k}\tanh(kD)},$$
$$c_g = \frac{c}{2}\left(1 + \frac{2kD}{\sinh(2kD)}\right).$$

This gives a relation between both the phase velocity c and the group velocity c_g and the wavenumber (Garnier et al. 2006, Mei 1989). Snell's law is used to relate the wavenumber to the wave angle, $\theta(x_1, x_2, t)$:

$$k\sin(\theta) = k^0 \sin(\theta^0), \tag{2.4}$$

with θ^0 and k^0 the wave angle and wavenumber at the offshore boundary respectively (Garnier et al. 2008). Finally, from linear wave theory, the instantaneous wave velocity $\mathbf{u^b}$ at the bed can be calculated.

2.3.2 Currents

The currents are modelled with the non-linear depth- and wave averaged shallow water equations in the Morfo55 model. This set of equations is formed by the mass conservation (2.5) and the momentum balance (2.6) described by Mei (1989):

$$\frac{\partial D}{\partial t} + \frac{\partial}{\partial x_j}(Dv_j) = 0, \tag{2.5}$$
$$\frac{\partial v_i}{\partial t} + v_j\frac{\partial v_i}{\partial x_j} = -g\frac{\partial z_s}{\partial x_i} - \frac{\tau_{bi}}{\rho D} - \frac{1}{\rho D}\frac{\partial}{\partial x_j}\left(S_{ij}^{'} - S_{ij}^{''}\right). \qquad i = (1,2) \tag{2.6}$$

Here, $D(x_1, x_2, t) = z_s - z_b$ is the total mean depth, z_s and z_b are the actual sea level and bed level respectively, ρ is the water density (1024 kg m^{-3}) and g is the gravitational acceleration (9.8 m s^{-2}). In these equations, the coupling between the waves and the current is parametrised by components of the stress tensor $\boldsymbol{S^{'}}$ and the time-averaged bed shear stress vector $\boldsymbol{\tau_b}$ (Mei 1989). The components $S_{ij}^{'}$ of the wave radiation stress tensor describe the net transport of i-momentum by wave in the j-direction (Longuet-Higgins and Stewart 1964). The components $S_{ij}^{''}$ of the turbulent Reynolds stress tensor give the input of turbulent part of the momentum equation (2.6). The components of the stress tensors and the stress vector are defined as

$$S_{ij}^{'} = E\left(\frac{c_g}{c}\frac{k_i k_j}{k^2} + \left(\frac{c_g}{c} - \frac{1}{2}\right)\delta_{ij}\right),$$
$$S_{ij}^{''} = \rho\nu_t D\left(\frac{\partial v_i}{\partial x_j} + \frac{\partial v_j}{\partial x_i}\right),$$
$$\boldsymbol{\tau_b} = \frac{1}{T}\int_0^T\left(\int_0^\infty \rho c_d|\boldsymbol{v} + \boldsymbol{u}^b|(\boldsymbol{v} + \boldsymbol{u}^b)P(H)dH\right)dt.$$

Here, c_g is the modulus of the group velocity vector of the waves, c is the modulus of the phase velocity of the waves, both given in section 2.3.1.Furthermore, k is the modulus of the wave number vector $\boldsymbol{k}$ and δ_{ij} is the Kronecker delta. The horizontal eddy viscosity coefficient, ν_t, is parametrized by MUL with M a constant (set to 1), U the velocity scale and L the length scale. In this case, the parametrisation has been done by Battjes (1975) . This links the velocity scale to the wave energy dissipation rate ε_b and the density by $U = (\varepsilon_b/\rho)^{1/3}$. The length scale has been parametrized with the root-mean square wave height H_{rms}, leading to the expression $\nu_t = M\,(\varepsilon_b/\rho)^{1/3}\,H_{rms}$. Furthermore, bed shear stress$\boldsymbol{\tau_b}$ is averaged over the wave period T. A probability distribution $P(H)$ is used to average over the wave amplitudes H. The bottom drag coefficient is denoted by c_d and $\boldsymbol{u}^b$ is the instantaneous total flow velocity at the bed.
So now there are 6 equations (2.2-2.6) and 6 unknown variables: $z_s(x_1, x_2, t)$, $v_1(x_1, x_2, t)$, $v_2(x_1, x_2, t)$, $E(x_1, x_2, t)$, $\sigma(x_1, x_2, t)$ and $\theta(x_1, x_2, t)$. This gives a closed set of equations which can be solved.

2.3.3 Sediment transport

The sediment transport is parametrised with the horizontal sediment transport flux $\boldsymbol{q}$ in $\mathrm{m}^3/(\mathrm{ms})$. For these simulations, the formulation of the sediment transport by Soulsby (1997) called Soulsby-Van Rijn has been used:

$$q_i = \alpha \left(v_i - \gamma u_{rms}^b \frac{\partial h}{\partial x_i} \right). \tag{2.7}$$

In this equation, γ is the bed slope coefficient and h is the bed level perturbation as defined in section 2.2. The root-mean square wave orbital velocity amplitude $u_{rms}^b = (\sigma H_{rms})/(2\sinh(kD))$ Soulsby (1997). Furthermore, α is the stirring factor given by

$$\alpha = A_s \left[\left(|v|^2 + \frac{0.018}{C_D} (u_{rms}^b)^2 \right)^{1/2} - u_{crit} \right]^{2.4}. \tag{2.8}$$

If the term in the squared brackets is positive, otherwise $\alpha = 0$ (Garnier et al. 2006). The constant $A_s = A_S + A_{SB}$ comprises the suspended load and bedload and depends on the sediment characteristics (Soulsby 1997). The smaller sediment particles (silt, clay, fine sand) are uplifted by the water and do not touch the bed level during transport. The larger and heavier particles travel over the sea bed and are therefore called bedload. These particles can either jump from one location to another (saltation), they can slide over the bottom or they can roll. These processes are showed in Figure 11. The velocity of the current must exceed the critical velocity u_{crit} for sediment transport to take place. For an increase of the velocity, the stirring factor increases and is a measure of the amount of sediment can be carried by the current. Furthermore, C_D is the morphodynamic, bottom drag coefficient and defined as $C_D = (0.40/\ln(D/z_0) - 1)^2$, with z_0 the initial bottom level.

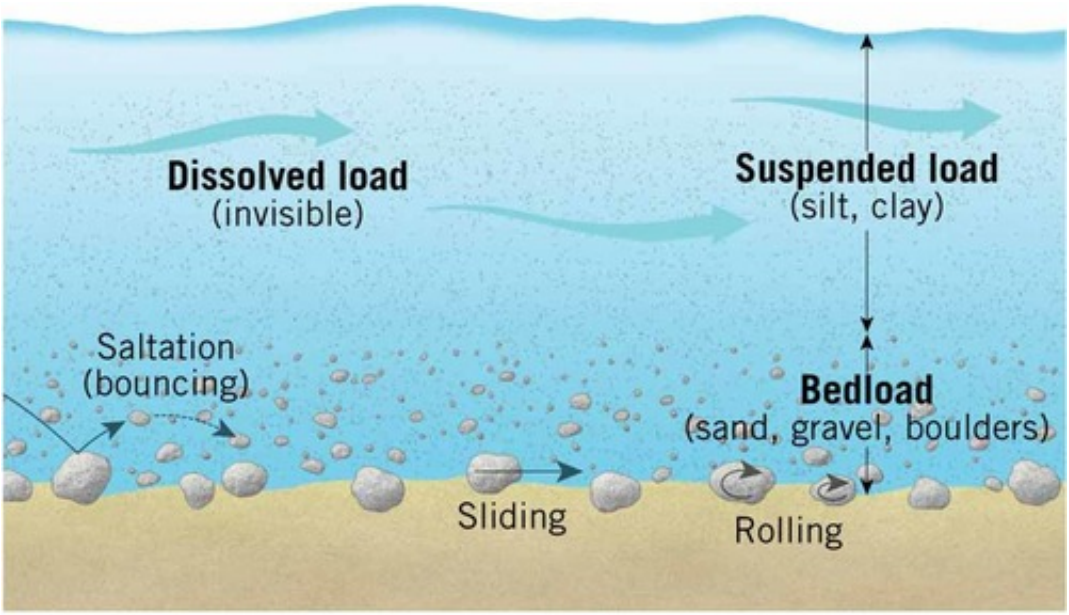

Figure 11: The process of sediment transport either in dissolved load, suspended load, or bedload. Suspended load are the smaller particles that can be uplifted by the water. The larger, heavier particles touch the bed during transport and are called bedload. When particles are light enough to be uplifted for small amounts of time, they can jump a small distance before gravity pulls them down again. Other particles glide over the bed and some roll in the direction of the flow. Figure from https://quizlet.com.

2.3.4 Bed evolution

The bed evolution of the system is modelled with the sediment mass conservation equation:

$$\frac{\partial h}{\partial t} + \frac{1}{1-p}\frac{\partial q_j}{\partial x_j} = 0. \tag{2.9}$$

This equation describes the coupling between the evolution of the perturbations in the bed level $h = z_b - z_b^0$ and the horizontal sediment transport flux $\boldsymbol{q}$. The sediment porosity p depends on the composition of the sea bed, in this case mainly sand grains (Garnier et al. 2006, Price et al. 2013).

2.4 Boundary conditions

On the edges of the domain, given in section 2.1, boundary conditions are imposed. Periodic boundary conditions have been assumed on the lateral boundaries, $y = 0$ and $y = L_y$ for D, $\boldsymbol{v}$, H_{rms}, θ and h. Meaning that these values and their derivatives are the same at $(x, 0, t)$ and (x, L_y, t).

At the shore boundary, $x = 0$, the water depth is set to $a_0 < 0$; thus, the backshore is not incorporated in this model. The velocity components of $\boldsymbol{v}$ and the sediment transport normal to the coast are zero at the shore boundary, so there is also no interaction between the nearshore zone and the backshore zone. Erosion and expansion of the coast are not taken into account. Note that, $H_{rms}(0, y, t)$, $z_b(0, y, t)$ and $z_s(0, y, t)$ can vary freely within the boundaries of the governing equations.

At the offshore boundary, the root-mean square wave height H_{rms} the angle θ^0 and the intrinsic frequency σ are imposed. These values are input parameters of the model, H_{rms} and θ^0 can be set periodically in time, but only with an imposed amplitude A and period T as

$$H^0_{rms} = A_H \sin(\frac{2\pi t}{T_H}) + H^0_{rms},$$
$$\theta^0 = A_\theta \sin(\frac{2\pi t}{T_\theta}) + \theta^0_0.$$

Here, H^0_{rms} is the mean wave height and θ^0_0 the mean angle of incidence. The actual water level z_s and bed level z_b are bounded by linear interpolation, $\partial^2 z_b / dx^2 = 0$. The velocities are set to decay exponentially from the offshore boundary in the direction of the coast.

2.5 Numerical aspects

The closed set of six equations (2.2-2.6 + 2.9) and the six unknowns can be solved. The model does this by using a rectangular staggered grid to descretise the domain in cells with size $(\Delta x, \Delta y)$ in the cross shore and longshore direction respectively. These grid sizes are defined as $(\Delta x, \Delta y) = \left(\frac{L_x}{N_x - 1}, \frac{L_y}{N_y}\right)$, with the number of computational point in the domain given by (N_x, N_y).

The computational domain, together with the locations at which vectors and scalars, are calculated and shown in Figure 12. The scalar variables are determined in the middle of these grid cells, the red dot in Figure 12, i.e. at $(x_i, y_1) = ((i - \frac{1}{2})\Delta x, (j - \frac{1}{2})\Delta y)$. The vectors fields are calculated at the boundaries of the cells. The cross-shore components of the vectors are defined at $(x_i, y_i) = \big((i-1)\Delta x, (j - \frac{1}{2})\Delta y\big)$, and the longshore components are defined at $(x_i, y_i) = \big((i - \frac{1}{2})\Delta x, (j-1)\Delta y\big)$ denoted by the blue and green dot in Figure 12 respectively. Here, $i = 1, ..., N_x$ and $j = 0, ..., N_y$ (Caballeria et al. 2002).

Time has also been discretised in small time steps Δt with $\Delta t = \Delta x \cdot qtx$. Here qtx is an input parameters of the model. The total amount of time that passed, is defined as $t_n = n\Delta t Moac$ with n an integer between $n = 0, ..., N_t$. Here, N_t is the maximum number of iterations done by the model. The Moac is a morphological acceleration factor used to speed up the morphodynamical processes. The time integration is performed by

a second-order Adams–Bashforth scheme (Bashforth and Adams 1883), except for the initial integration between $N_t = 0$ and $N_t = 1$. This step is modelled with the Euler first-order scheme.
‘

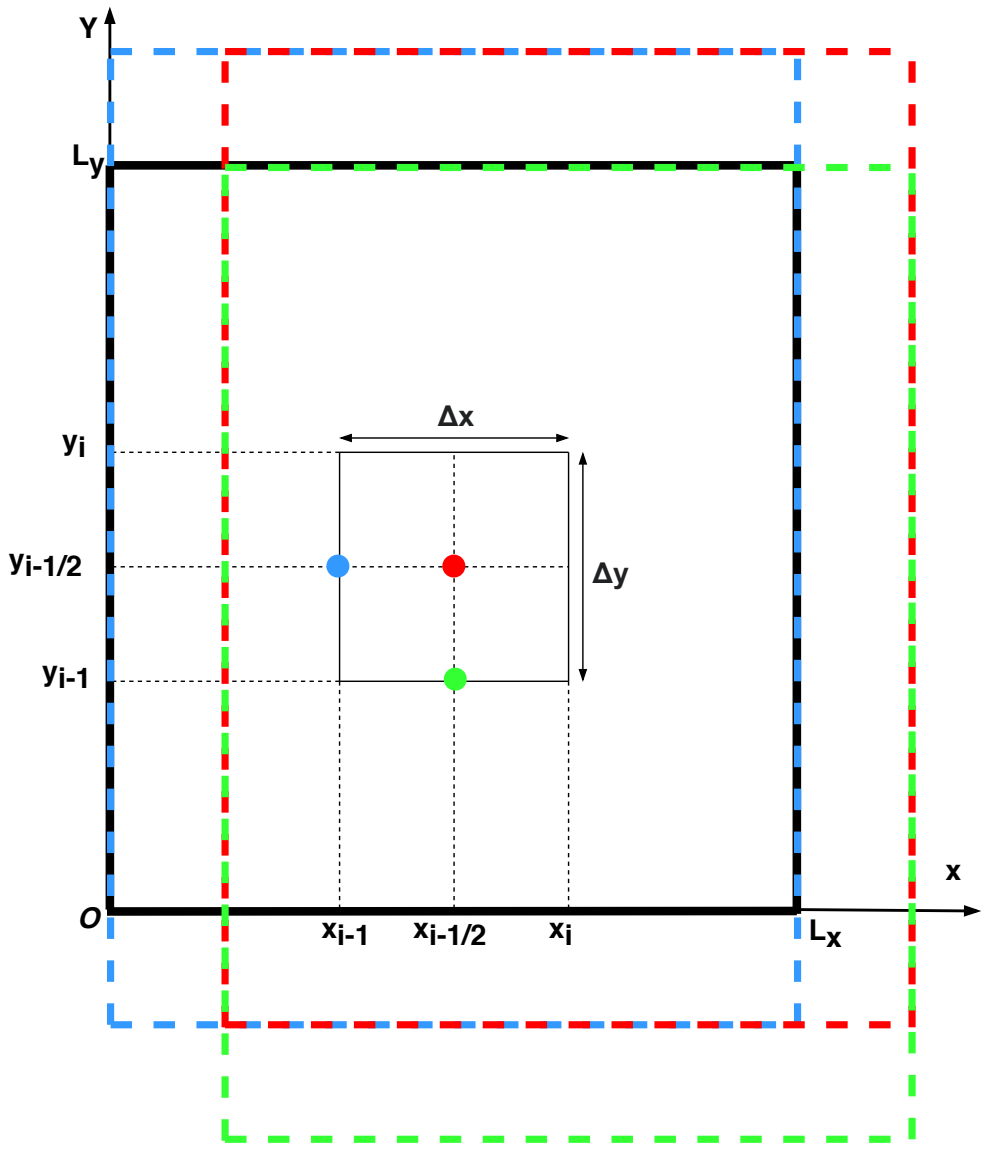

Figure 12: Computational domain with a schematic overview of the staggered grid. The location where the scalars, cross-shore components of the vectors and longshore components of vectors are calculated are given by the red dot, the blue dot and the green dot respectively. The computational domains of the scalars and vector components are given in matching colours.

3 Method

3.1 Parameters

To be able to start the simulations, the input parameters need to be chosen. The domain of the model is set to $0 < x < L_x$ with $L_x = 250$ m and $0 < y < L_y$ with $L_y = 1500$ m. This domain is chosen so that both uniform shore-parallel bars are fully inside the domain and that in the longshore direction multiple alternating horns and bays can be simulated. This is based on the domain of Garnier et al. (2006). The bed profile has been chosen such that it resembles the profile used by Price et al. (2013). A list of these parameters is given in Table 1.

The hydrodynamical and sediment parameters have been chosen to be the same as in Garnier et al. (2006). A list of all these parameters is provided in Table 2. The wave angle θ^0 at the offshore boundary does not have a fixed value. Many experiments will have periodically time-varying angles. The numerical parameters used for the calculations done by Morfo55, given in Section 2.5, are provided in Table 3.

Symbol	description	value
Domain		
L_x	cross-shore domain length	250 m
L_y	longshore domain length	1500 m
Profile		
a_0	depth at coastal boundary	0.25 m
a_1	form of the slope	2.97
β_1	slope first part bottom	0.034
β_2	slope of second part bottom	0.0245
c_1	amplitude inner bar	0.8 m
c_2	amplitude outer bar	2.36 m
x_1	position inner bar	40.8 m
x_2	position outer bar	140.8 m
w_1	width inner bar	20 m
w_2	width outer bar	40 m

Table 1: List of parameters used for the domain and bed profile. The left, middle and right column list the symbols used in this report, a short description of their meanings and the value which is used in the simulations respectively.

Symbol	description	value
Hydrodynamics		
ρ	water density	1024 kgm^{-3}
κ	velocity decay parameter	3
H^0_{rms}	wave height at offshore boundary	1.5 m
T	wave period	9 s
γ_b	wave breaker index	0.6
c_d	hydrodynamical drag coefficient	0.01
Sediment		
γ	bedslope parameter	10
z_0	roughness length	0.02 m
d_{50}	particle size	0.00025 m
p	sediment porosity	0.4
s	relative sediment density	2.65

Table 2: List of all physical parameters. The left, middle and right column give the symbols used in this report, a short description of their meanings and the value which is used in the simulations respectively.

symbol	description	value
Numerics		
Δx	cross-shore grid size	5 m
Δy	longshore gridsize	20 m
Δt	time step	0.05 s
qtx	qtx = $\Delta t/\Delta x$	0.01
Moac	morphological acceleration factor	90

Table 3: List of numerical parameters. The left, middle and right column give the symbols used in this report, a short description of their meanings and the value which is used in the simulations respectively.

3.2 Experiments

In order to find the response of a double-barred beach system to time-varying wave angles, a set of experiments have been executed for periodically time-varying wave angles according to

$$\theta^0 = A_\theta \sin(\frac{2\pi t}{T_\theta}) + \theta_0^0. \tag{3.1}$$

Here, θ_0^0 is the mean angle of incidence, T_θ the period over which the angle varies and A_θ the maximum variations of the amplitude around θ_0^0. The first set focusses on the influence of periodically varying wave angles with a mean angle normal to the coast, $\theta_0^0 = 0^o$. The second set of simulations has the same variables, but for an oblique mean angle, $\theta_0^0 = 4^o$. The experiments are named and described in Table 4.

3.2.1 Normal wave incidence

The experiments with normal incidence are denoted by Run1-Run4T. Run1 has constant offshore wave conditions and normal incidence. This is the reference case of the experiment. Run2T is a series of experiments with time-varying angles around $\theta_0^0 = 0^o$ with a maximum amplitude of $A_\theta = 3^o$ for different periods, $T_\theta =$ 2.5, 5, 7.5, 10, 15, 20 and 25 days. A similar series has been performed for a maximum amplitude of $A_\theta = 6^o$, denoted by Run3T, and for maximum amplitude of $A_\theta = 9^o$, denoted as Run4T. These sets of experiments enable an analysis of the response of the double-barred system to different periods by comparing the different cases within a set of experiments. They also allow for an analysis of the influence of amplitude of the angles on the response of the system. To do this, the simulations of Run2T, Run3T and Run4T will be compared for the same period.

3.2.2 Oblique wave incidence

Most of the time, the wave angle of incidence for straight beaches is not normal to the coast. That is why a third subquestion was formulated, regarding the influence of sinusoidally varying angle with an oblique mean angle. A series of simulations, for which waves at the offshore boundary have oblique mean angles, have been done, these experiments have been named Run5-Run8T. Run5 has constant wave conditions for a mean angle of incidence $\theta^0 = 4^o$, which is the reference case. Run6T has periodically varying angles of incidence with the same mean angle $\theta^0 = 4^o$, an amplitude $A_\theta = 3^o$ and periods $T_\theta = 2.5$, 5, 7.5, 10, 15, 20 and 25 days. A similar series of experiments has been performed for amplitudes $A_\theta = 6^o$ and $A_\theta = 9^o$, Run7T and Run8T respectively. The same analysis as described in the section above for mean incidence normal to the coast was done for these oblique waves.

Run name	Description
Run1	$\theta_0^0 = \theta^0 = 0^o$
Run2T	$\theta_0^0 = 0^o$ $A_\theta = 3^o$ T_θ = 2.5, 5, 7.5, 10, 15, 20, 25 days
Run3T	$\theta_0^0 = 0^o$ $A_\theta = 6^o$ T_θ = 2.5, 5, 7.5, 10, 15, 20, 25 days
Run4T	$\theta_0^0 = 0^o$ $A_\theta = 9^o$ T_θ = 2.5, 5, 7.5, 10, 15, 20, 25 days
Run5	$\theta_0^0 = \theta^0 = 4^o$
Run6T	$\theta_0^0 = 4^o$ $A_\theta = 3^o$ T_θ = 2.5, 5, 7.5, 10, 15, 20, 25 days
Run7T	$\theta_0^0 = 4^o$ $A_\theta = 6^o$ T_θ = 2.5, 5, 7.5, 10, 15, 20, 25 days
Run8T	$\theta_0^0 = 4^o$ $A_\theta = 9^o$ T_θ = 2.5, 5, 7.5, 10, 15, 20, 25 days

Table 4: List of Runs executed in this study. Here, θ^0 is the angle of incidence at the offshore boundary, θ_0^0 is the mean angle of incidence at the offshore boundary, A_θ is the maximum amplitude with which the angle can vary around θ_0^0. Finally, T_θ is the forcing period with which the angle is varied. Values of all other parameters are presented in Table 1-3.

3.3 Analysis

3.3.1 3D bottom profile

The first method to analyse the response of the double-barred beach system to different hydrodynamics was done by plotting perturbations $h(x_1, x_2, t)$ in the bed level as a function of the position. With the cross-shore distance on the horizontal axis and the longshore distance on the vertical axis, the perturbations, h, was plotted as an contour plot for every grid cell. This gives the actual bed profile for a one time shot, but with multiple time frames after the other, a short animation was made. A similar analysis was done for the actual bed level $z_b(x_1, x_2, t)$ instead of the perturbations. This analysis gave insight into the coupling between the inner and outer bar, but it made it hard to compare different simulations.

3.3.2 2D time evolution of bed level at longshore sections

While the first method of analysis gives a 3D evolution of the domain, it was difficult to compare results from different cases. The time evolution of the the bed level at longshore sections was plotted, resulting in a 2D representation of the data at a fixed section. This way, one could consider bottom perturbations at a fixed section of the domain, while there were still 2D patterns visible and, in contrast to 3D patterns, they were shown as a continuous function of time. A longshore section of the domain could be taken at any given position x = constant. The most interesting locations are section that lie over the inner or outer bar around x_{lss1} = 40 m and x_{lss2} = 140 m. Two of these sections were output of the simulations for every time step

and could thus be plotted as a function of time. This method of displaying the data enabled us to follow the growth, change position end merging or splitting of the bars for every time-step in one figure. When also plotting the periodic variation of either the wave height H_{rms} or the angle of incidence θ^0, the coupling between these parameters and the growth rate and change position could easily be seen.

3.3.3 1D time evolution of the root-mean square bar height

Plotting the time evolution of the root-mean square bar height $||h||(t)$, defined as

$$||h|| = \left(\frac{1}{L_x L_y} \int_0^{L_x} \int_0^{L_y} h^2 dy dx \right)^{1/2}, \tag{3.2}$$

facilitated the investigation of results. When using this method information about the 3D patterns was lost and only a 1D representation remained. This gave an averaged perturbation of the bottom over the whole domain at a fixed moment in time (Garnier et al. 2006). Because there are two uniform shore-parallel bars in the domain, with different dynamics in their vicinity, it is useful to average the perturbation over two different subdomains, so that the morphodynamics of in these two domains could be analysed separately. This led to the expressions

$$||h||_{Inn} = \left(\frac{1}{x_h L_y} \int_0^{x_h} \int_0^{L_y} h^2 dy dx \right)^{1/2}, \tag{3.3}$$

$$||h||_{Out} = \left(\frac{1}{(L_x - x_h) L_y} \int_{x_h}^{L_x} \int_0^{L_y} h^2 dy dx \right)^{1/2}, \tag{3.4}$$

with the boundary between the two domains halfway between the two shore-parallel bars at $x_h = 90$ m (see also Table 5). For every time step, $||h||$ was determined and plotted as a function of the time. Information about the presence of an equilibrium in the mean bar growth was investigated with this information. The influence of different hydrodynamical conditions on the bars grow was investigated as well.

The root-mean square bar height was further analysed by calculating the period and amplitude of the variations in the function. The former was done by a discrete-time Fourier transformation as described below. The latter was done by a calculation of the standard deviation of the mean. A fit with a cubic polynomial through the data of $||h||$ was made to determine the mean, $||h||_{av}(t)$ between $t = 20$ and 80 days. Next the standard deviation was calculated as

$$\sigma_{||h||} = \sqrt{\frac{1}{N_t} \sum_{t_{\min}}^{t_{\max}} \left(||h||_{av}(t) - ||h||(t) \right)^2}. \tag{3.5}$$

Here, N_t is the number of time steps defined as $N_t = (t_{\max} - t_{\min}) / \Delta t$.

3.3.4 Fourier analysis

A discrete Fourier transformation in space can be performed on the longshore section of the domain as described above. This method enables us to find the dominant wavelength, λ_m, of the alternating pattern of shoals and troughs at every time step. In this way, information is obtained about the temporal behaviour of the dominant length scales of the bars. This transformation is performed as

$$\mathcal{H}(k_l) = \sum_{j=1}^{N_y} h(x_{lss}, y_j) \exp\left(-i \frac{2\pi}{N_y} (j-1)(l-1) \right). \tag{3.6}$$

In this expression, $k_l = \frac{2\pi(l-1)}{L_y}$, the wavenumber and its corresponding Fourier coefficient is $\mathcal{H}(k_l)$, with $l = 1 : N_y$, the mode of the Fourier transformation. Furthermore, $N_y = L_y / \Delta y$ is the number of computational point on the vertical axis, x_{lss} is the cross-shore position of the longshore section where the Fourier

transformation is done, in this case either x_{lss1} or x_{lss}. The position of along the horizontal axis is given by $y_i = j\Delta y$ (Garnier et al. 2006). The dominant wavelength, λ_m, between the adjacent bars is obtained by rewriting the expression for the dominant wavenumber, $k_m = 2\pi/\lambda_m$ with $\lambda_l = L_y/(l-1)$. The expression for the Fourier coefficient is complex, so a scaled power was used for the representation of the data. The scaled discrete power $P(\lambda_l) = |\mathcal{H}(k_l)|^2/|\mathcal{H}_{max}|^2$ was plotted as a function of the wavelength $\lambda_l = 2\pi/k_l$.

A similar analysis is performed for a discrete-time Fourier transform for the root-mean square bar height $||h||(t)$. This leads to a dominant period in the variations of $||h||$ in the outer or inner domain. The transformation is performed as

$$||\mathcal{H}||(\omega_n) = \sum_{j=1}^{N_t} ||h||(t_j) \exp\left(-i\frac{2\pi}{N_t}(j-1)(n-1)\right). \tag{3.7}$$

In this expression, ω_n is the frequency and its corresponding Fourier coefficient is $\mathcal{H}(w_n)$, with $n = 1 : \frac{1}{2}N_t$, the mode of the Fourier transformation. Furthermore, $||h||$ is either $||h||_{Inn}$ or $||h||_{Out}$, N_t is the total number of time steps taken into account and the moment in time $t_j = j\Delta t$.

The Fourier coefficient is again complex, so the scaled discrete power, $P(T) = |\mathcal{H}(\omega_n)|^2/|\mathcal{H}_{max}|^2$ is plotted as a function of the period $T = 2\pi/\omega$.

symbol	description	value
analysis		
x_h	the boundary between the domain of the inner and outer bar	90 m
x_{lss1}	location of longshore section 1 (over innerbar)	40 m
x_{lss2}	location of longshore section 2 (over outerbar)	140 m

Table 5: A table of the variables used to divide the domain or set a location for analysis.

4 Results

4.1 Normal wave incidence

4.1.1 Reference case

The output of the reference case, Run1, is compared to that of Run2T$_{10}$, the simulation with time-varying angles with a mean angle of $\theta_0^0 = 0^o$ and a period $T_\theta = 10$ days. Snapshots of the 3D bottom patterns at different times are given in Figure 13. The left column of this figure shows the actual bottom level z_b and the bottom perturbation h for Run1, while the right column shows the patterns for Run2T$_{10}$. The panels b-e and g-k show approximately a full period of the variation in wave angle.

Run1 shows a very regular crescentic pattern that does not change much in time and space. The patterns in the outer domain show an alongshore variation in depth at a wavelength twice the wavelength of the alongshore variations in the inner domain. When there is a horn around $x = 130$ meters (outer domain) there is always a bay around $x = 40$ meters (inner domain). They are almost connected by a bulge of the horn toward the coast. Run2T$_{10}$ shows a less regular pattern, but there is still a slight bay in the inner domain when there is a horn in the outer domain in Figure 13 h-l. The patterns in the inner domain are smaller than those in the outer domain.

The 2D longshore sections in Figure 14 show the bottom perturbation h at $x = 40$ m and $x = 140$ m as a function of time for Run1 in the left column and for Run2T$_{10}$ in the right column. The red colours indicate an elevation on top of the shore parallel bars and the blue colours indicate a depression. The vertical lines coincide with the time of the snap shots in Figure 13. The bars of Run1 show no merging or splitting and only grow in time. In contrast, the bars of Run2T$_{10}$ do show merging and splitting and show both an increase and a decrease in bar height.

The vertical line at $t = 15$ days show that the bars in the outer domain are not fully developed yet, at this point the inner bars still show a regular pattern. This pattern starts to change when the bars in the outer domain start to develop. This corresponds with the observations as shown in Figure 13.

Figure 15 shows the time evolution of the scaled discrete power of the Fourier coefficients at x=40 m (inner domain) and at x=140 m (outer domain) of Run1 in the left column and Run2T$_{10}$ in the right column. The sediment transport starts at $t = 2.6$ days, before this time, the perturbations in the domain are random, which explains the band of colour between $t = 0$ and $t = 2.6$ days. The figure reveals that the dominant wavelength of Run1 in the inner domain is approximately 150 meters and in the outer domain 300 meters. Thus, there are twice as many bars in the longshore direction in the inner domain than in the outer domain. For Run2T$_{10}$, this is more complicated. There are multiple dominant wavelengths in both the inner and outer domain.

As can be seen from Figure 16, the growth of the perturbations on the outer uniform bar is delayed by a few days with respect to the growth in the inner domain. This delay is larger for the case with a time-varying angle of incidence. The latter case shows oscillations in the root-mean square bar height $||h||$ which the reference case does not show. The mean bar height, $||h||_{av}(t)$, in the outer domain is for both cases approximately the same and larger than those in the inner domain. The mean bar height, $||h||_{av}(t)$, in the inner is largest for the reference case with constant wave angle.

The scaled discrete temporal power spectra of the Fourier coefficient shown in the top panels of Figure 17, reveal that the dominant period of Run2T$_{10}$ $T_{||h||}$ is 5 days for both the inner and outer domain. Thus, the dominant period of the response is half of that of the forcing. The difference between the mean and the actual $||h||$ is shown in the bottom panels of Figure 17. The standard deviation $\sigma_{||h||}$ of the mean trend is a measure of the amplitude of the time-varying response. Between $t = 20$ and $t = 85$ days, $\sigma_{||h||} = 0.01$ m and $\sigma_{||h||} = 0.023$ m for the inner and outer domain, respectively.

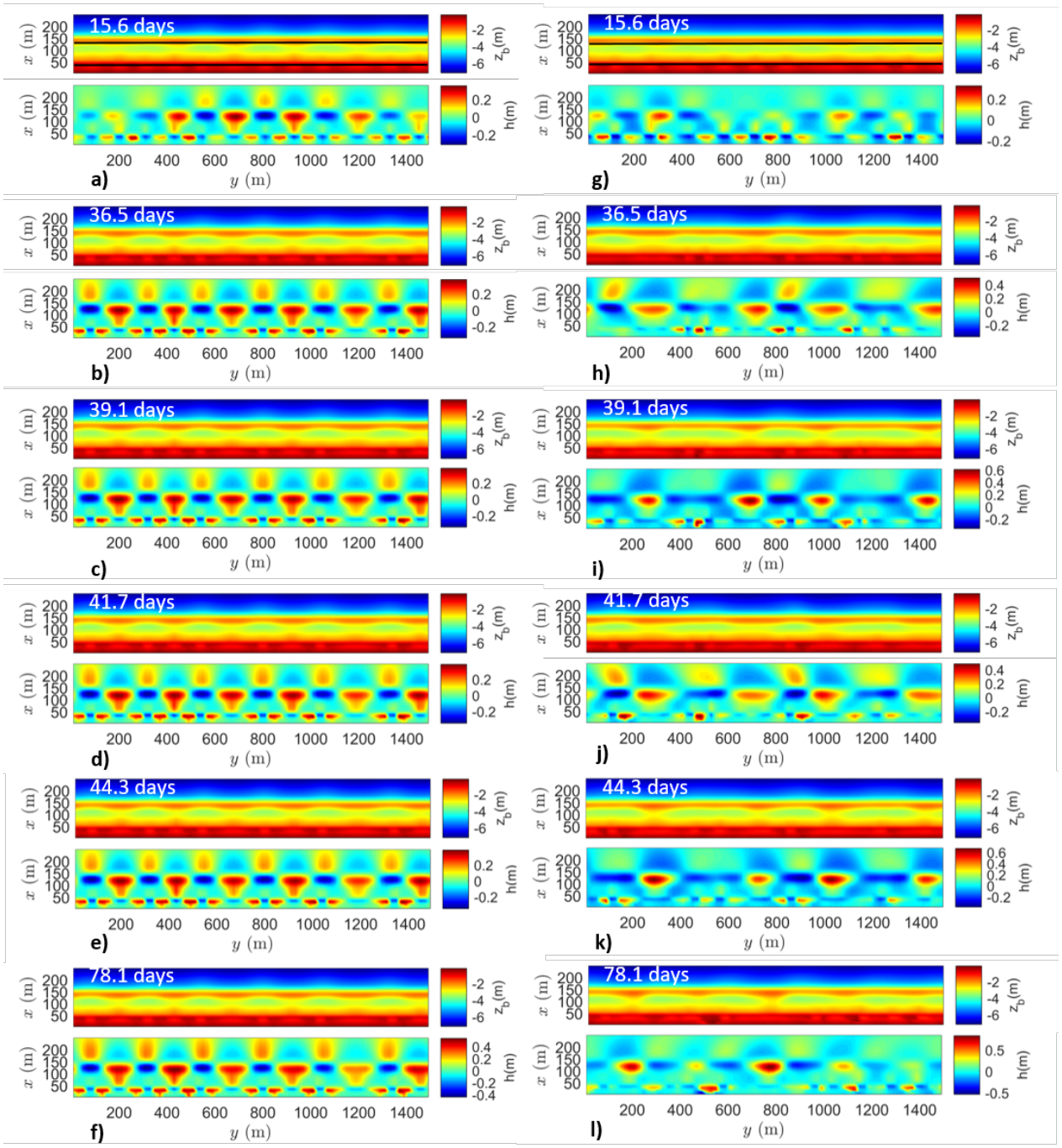

Figure 13: The actual bottom level z_b and the bottom perturbation h are plotted as a function of the position in the domain. This is done for Run1 (constant angle with a mean angle of $\theta_0^0 = 0^o$) in the left column (a-f) and for Run2T$_{10}$ (time-varying angle with $\theta_0^0 = 0^o$, $A_\theta = 3^o$ and $T_\theta = 10$ days) in the right column (g-l). For both cases, z_b and h are given for different five different moments in the simulation indicated in the figures. The longshore direction y and the cross-shore direction x are given in meters. The negative, blue, values in the lower plot indicate a position of erosion on the uniform bar whilst the positive, red, values indicate a position where sediment accumulates. The black lines in the upper figure, a) and g), denote the location of the longshore sections in Figure 14.

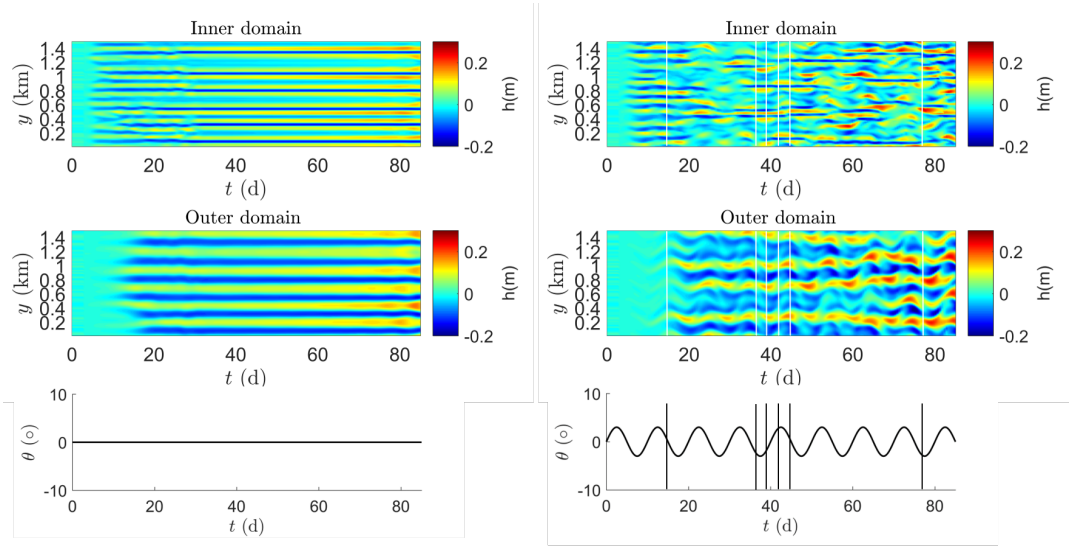

Figure 14: Left column: Run1 (constant wave forcing with $\theta_0^0 = 0^o$), right column: Run2T$_{10}$ (time-varying forcing with $\theta_0^0 = 0^o$, $A_\theta = 3^o$ and $T_\theta = 10$ days). The bottom perturbation along the longshore direction y in km is plotted as a function of time t in days. The section are taken at $x = 40$ m (inner bar) and at $x = 140$ m (outer bar), as indicated by the black lines in Figure 13. The angle of incidence at the offshore boundary is given below the longshore sections. The vertical lines in the longshore sections in the right column and the plot of the angle indicate the moments for which the bottom perturbations in Figure 13 are shown.

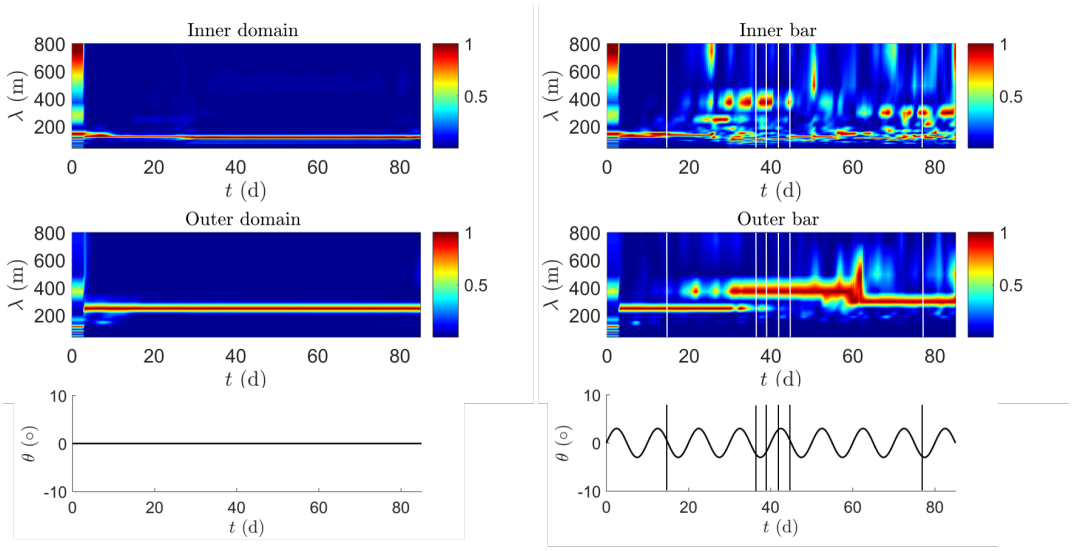

Figure 15: Time evolution of the scaled discrete power of the Fourier coefficients of $h(x, y, t)$ at x=40 m (inner domain) and x=40 m (outer domain), is shown for Run1 in the left column and Run2T$_{10}$ in the right column. The vertical axis gives the dominant wavelength in meters as a function of the time t in days on the horizontal axis. The angle of incidence at the offshore boundary as a function of time is plotted below the panels showing the spectra. The vertical lines in the right column and the plot of the angle indicate the moments for which the bottom perturbations in Figure 13 are shown.

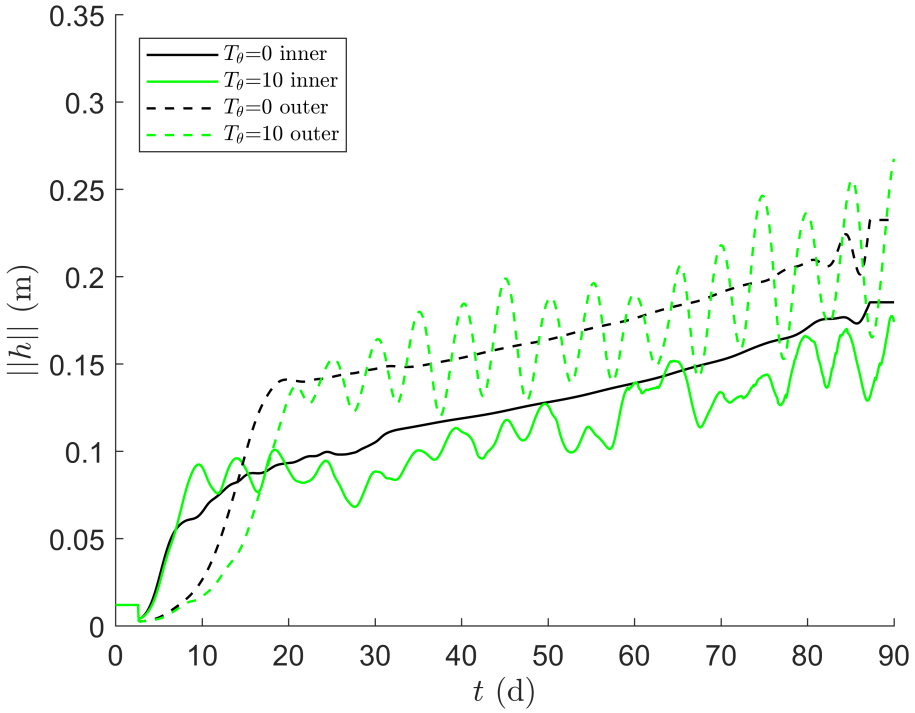

Figure 16: Root-mean square height of the bottom perturbations in meters as a function of the time in days. This is done for both the inner domain (solid line) and the outer domain (dashed line) for two different cases. The black line shows the results of the case with a period in wave angle of 0 days, so the wave angle is constant in time (Run1). The green line shows the results for the case with a period of 10 days in the wave angle and an amplitude $A_\theta = 3^o$ (Run2T$_{10}$).

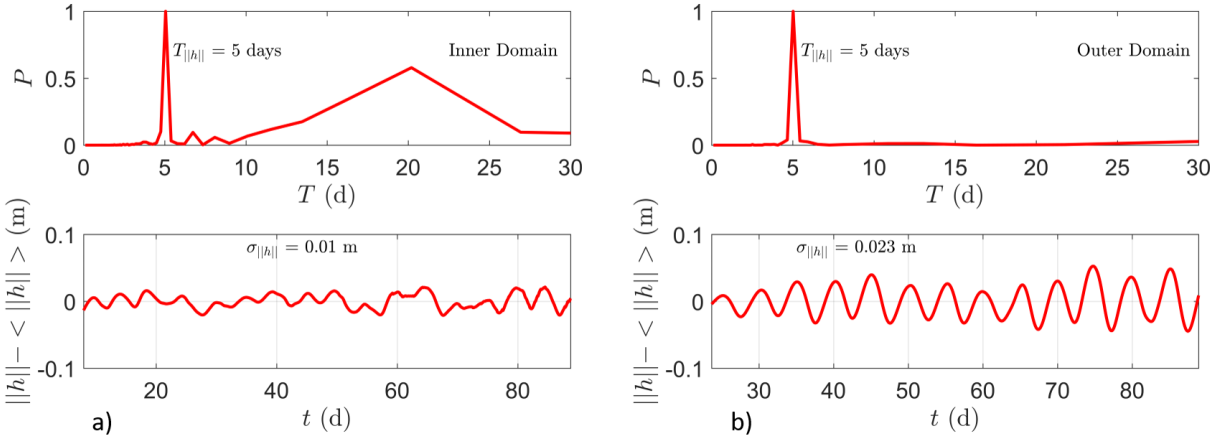

Figure 17: Upper panels: scaled discrete temporal power spectra of the function $||h||$ as shown in Figure 16 versus period (in days) for the inner domain (left) and outer domain (right), Run2T$_{10}$. Lower panels: time series of the residual root-mean square bar height with respect to its running mean ¡——h——¿.

4.1.2 Sensitivity to different forcing periods

The simulations were also done for T_θ = 2.5, 5, 7.5, 10, 15, 20 and 25 days and $A_\theta = 3^o$, Run2T. These cases all display a crescentic bar pattern in both the inner and outer domain similar to the Run2T$_{10}$. Again, with smaller patterns in the inner domain than the outer domain. The patterns are also less regular than for Run1, which can also be seen in Appendix A Figure 27.

The bars alternate between moving in the positive and negative longshore direction. With increasing forcing period of the wave angle, bars keep moving longer in the same direction. The number of bars is approximately the same in all cases and does not show any correlation with the period of the angle. The time at which they start to grow is also the same for al three cases shown in Figure 27. In the inner domain, growth starts after approximately 5 days, while the bars in the outer domain start growing after 15 days. Merging and splitting occurs in both the inner and outer domain for all periods from the moment bars start to form in the outer domain. The colours on the outer bars are more extreme than on the inner bar, indicating a larger growth on the outer bar.

The difference in growth-rate on the inner and outer bar is also apparent in the time series of the root-mean square bar height $||h||$ (see Appendix A, Figure 28-30). The bars in the inner domain remain smaller than in the outer domain. The fit through $||h||(t)$ is always lower for time-varying waves in the inner domain. A such, the time-varying wave angles cause the bars in the inner domain to grow slower. The smallest mean bar height $||h||_{av}(t)$ is seen for period $T = 2.5$ and 5 days, for period $5 < T \leq 25$ $||h||_{av}(t)$ starts to become larger again, but still lower than for Run1 (constant wave forcing). In the outer domain, this differences in $||h||_{av}(t)$ are not apparent, except for the forcing periods T_θ 2.5 days and 5 days. For these two cases, the mean bar height is significantly lower than for Run1 (constant wave forcing).

The period and standard deviation of $||h||(t)$ of these cases are shown in Figure 18 for the inner domain in the left column, a) and the outer domain in the right column b). They reveal an increase in the response period $T_{||h||}$ for an increase in the forcing period for the angle T_θ with $T_{||h||} = \frac{1}{2}T_\theta$ both in the inner and outer domain. The only exception is in the inner domain for $T_\theta = 5$ days where $T_{||h||} = T_\theta$. For a forcing period $T_\theta = 2.5$ days, the variations of $||h||(t)$ show multiple dominant periods in both the inner and outer domain. The standard deviation of the fit through $||h||(t)$ is higher in the outer domain than in the inner domain. Furthermore, $\sigma_{||h||}$ for $T_\theta \geq 10$ days is larger than $\sigma_{||h||}$ of the smaller periods ($T_\theta < 10$ days). A peak in the deviation appears for $T_\theta = 15$ days. This might indicate a resonance between forcing period and the response. Reasons for the $T_{||h||} = T_\theta/2$ peak and the occurrence of peaks in Figure 18 are given in the Section 5, the discussion.

4.1.3 Sensitivity to different forcing amplitudes

The influence of the amplitude with which the angle varies, A_θ, is quantified by analysing the differences between Run2T, Run3T and Run4T ($A_\theta = 3^o$, $A_\theta = 6^o$ and $A_\theta = 9^o$ respectively) for the same periods. The initial activity starts in the inner domain for all three cases. The activity in the outer domain starts at $t = 10$ days, $t = 20$ days cases Run2T$_{10}$ and Run3T$_{10}$ respectively. For Run4T$_{10}$ the activity in the outer domain is so small that it could not be seen, neither in the 3D bottom perturbation plot, nor in the 2D longshore sections (see Appendix A Figure 31). The initial pattern in the inner domain is very regular, until the bars in the outer domain start to grow.

An increase in the angle causes an increase in the time it takes for the outer bars to start to grow (see Appendix A, Figure 32). When the bars in the outer domain start to grow, the mean bar height $||h||_{av}(t)$ becomes larger than in the inner domain. An increase in the angle also causes a decrease in $||h||_{av}(t)$ for both domains.

The scaled discrete temporal power spectra of the Fourier coefficient of $||h||$ shows that for all amplitudes, the dominant period $T_{||h||} = \frac{1}{2}T_\theta$, with a less dominant period of $T_{||h||} = \frac{1}{4}T_\theta$. The inner bar also shows a less dominant period at $T_{||h||} = T_\theta$. The standard deviation of the fit through $||h||(t)$ did not significantly differ for the 3 cases. Therefore, it appears that there is no influence of the maximum amplitude of the incident waves on $T_{||h||}$ and $\sigma_{||h||}$.

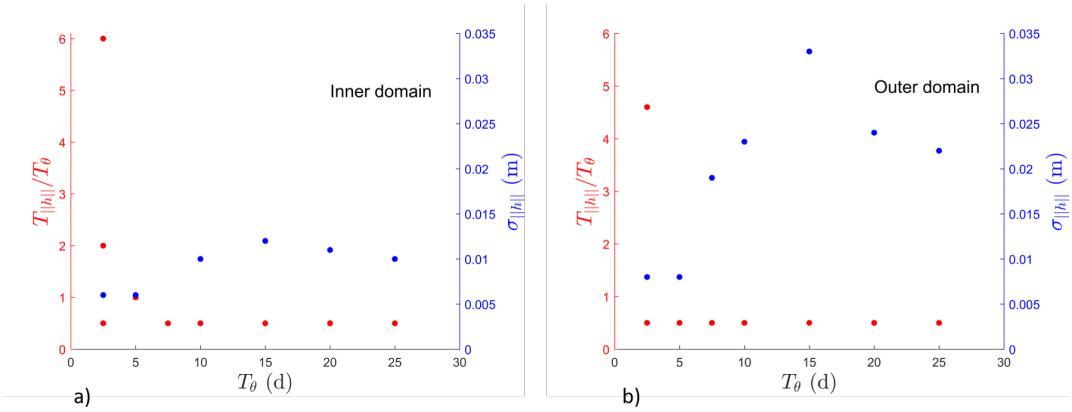

Figure 18: Dominant periods in the response $T_{||h||}$ scaled to the forcing period T_θ and the standard deviation $\sigma_{||h||}$ in meters of the root-mean square bar height $||h||$ on the left and right vertical axis respectively. The different forcing periods of wave angles T_θ (Run2T) for inner and outer domain are shown on the horizontal axis. The inner domain is shown in panel a) and the outer domain is shown in panel b). For $T_\theta = 2.5$ days, multiple response periods are found.

4.2 Oblique wave incidence

4.2.1 Reference case

The reference case of the simulations with a nonzero mean angle of wave incidence at the offshore boundary is given by Run5 (constant wave forcing) and compared to Run6T$_{10}$ (periodically varying wave angle). Snapshots of the 3D bottom patterns are presented in Figure 19. They show no bar activity on top of the outer longshore parallel uniform bar for the case with a constant angle of incidence, Run5 shown in the left column. The activity is focussed in the inner domain and shows a regular pattern in space and time. This pattern is not symmetric around an axis parallel to the cross-shore direction. It shows a slight shift of the patterns around $x = 80$ m in the positive longshore direction. Again, Figure 20 shows that, in the case of time-varying wave forcing, the bottom perturbations in the outer domain do in fact grow after 80 days. When there is a horn on the outer uniform bar, there is a bay on the inner uniform bar. Between the horn in the outer domain, large bays occur that are approximately twice as long as the horns. The number of bars in the inner domain is much larger than in the outer domain, which was also seen in the case of a mean angle normal to the coast.

In Figure 20, the evolution of bottom perturbations at two longshore sections are shown. These sections are taken at the location of the black lines indicated in Figure 19 a) and g). Figure 20 shows a shift in bar position in both the inner and outer domain for Run6T$_{10}$ after $t = 80$ days in the positive longshore direction. This is the same direction as that of the mean wave vector. The shift in position is largest for the largest angles. It starts when the wave angle at the offshore boundary has almost reached its max and stops when it is just over its maximum. This figure also shows that when the bars in the outer domain start to grow, the patterns in the inner domain become less regular. The time evolution of the scaled power as a function of wavelength of the bottom perturbation shown in Figure 21 indicates this transition around $t = 80$ days with a change in dominant wavelength of the bars in the inner domain. For $t < 80$ days, the dominant wavelength is very regular around $\lambda_m = 200$ meters while for $t > 80$ days, the dominant wavelength alternates in time.

The root-mean square bar height $||h||$ of Run5 and Run6T$_{10}$ is shown in Figure 22. The bar height in the inner domain is larger for a constant angle than for time-varying angles. The period and standard deviation in $||h||(t)$ of Run6T$_{10}$ are shown in Figure 23 a) and b) for the inner and outer domain respectively. The inner domain shows two dominant periods at $T_{||h||} = \frac{1}{2}T_\theta$ and $T_{||h||} = T_\theta$ the outer domain shows only one dominant response period at $T_{||h||} = T_\theta$.

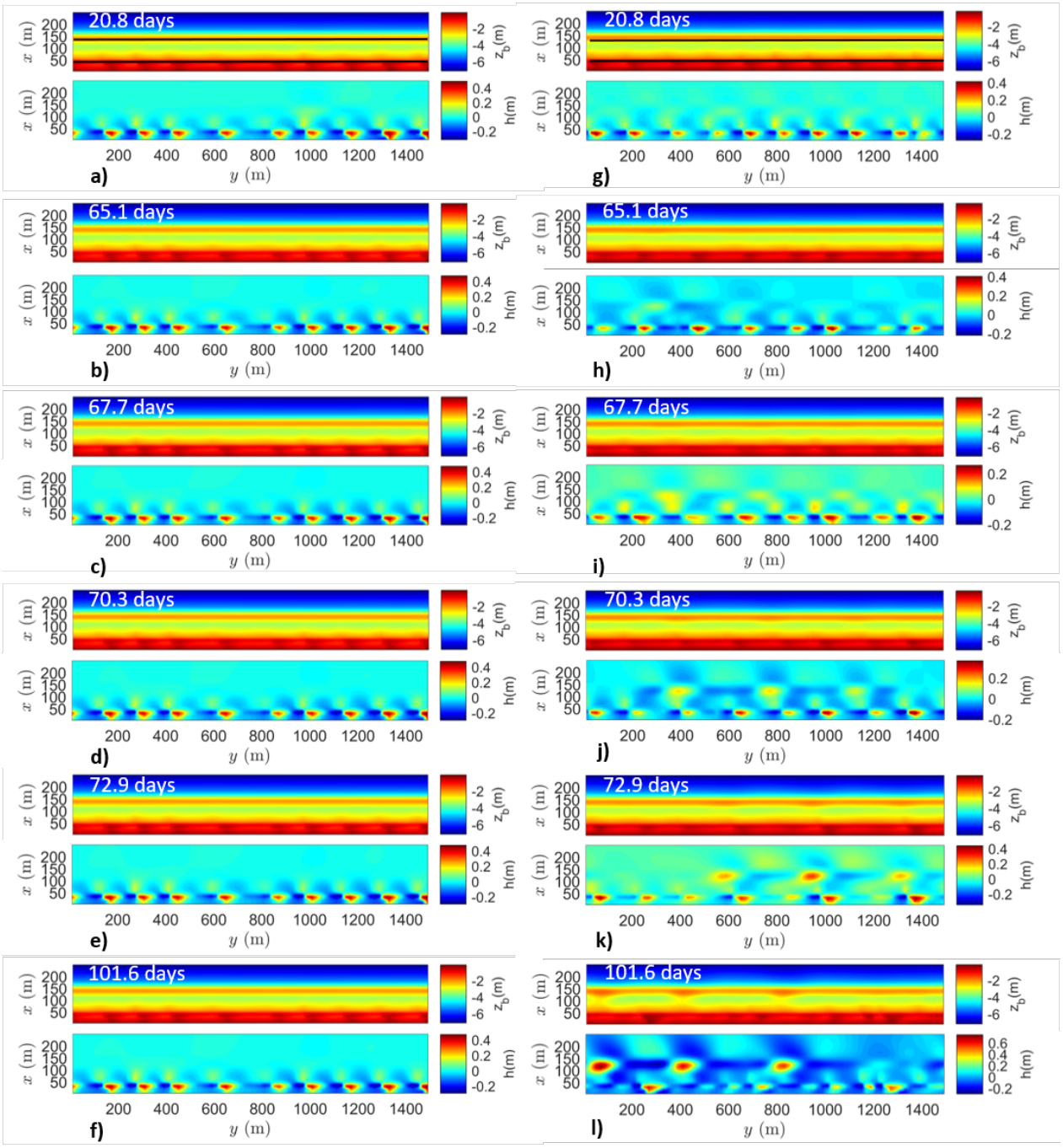

Figure 19: The actual bottom level z_b and the bottom perturbation h are plotted as a function of the position in the domain. This is done for Run4 (constant angle with a mean angle of $\theta_0^0 = 4^o$) in the left column (a-f) and for Run6T$_{10}$ (time-varying angle with $\theta_0^0 = 4^o$, $A_\theta = 3^o$ and $T_\theta = 10$ days) in the right column (g-l). For both cases, z_b and h are given for different five different moments in the simulation indicated in the figures. The longshore direction y and the cross-shore direction x are given in meters. The negative (blue) values in the lower plot indicate a position of erosion on the uniform bar whilst the positive (red) values indicate a position where sediment accumulates. The black lines in the upper figure, a) and g), denote the location of the longshore sections in Figure 20.

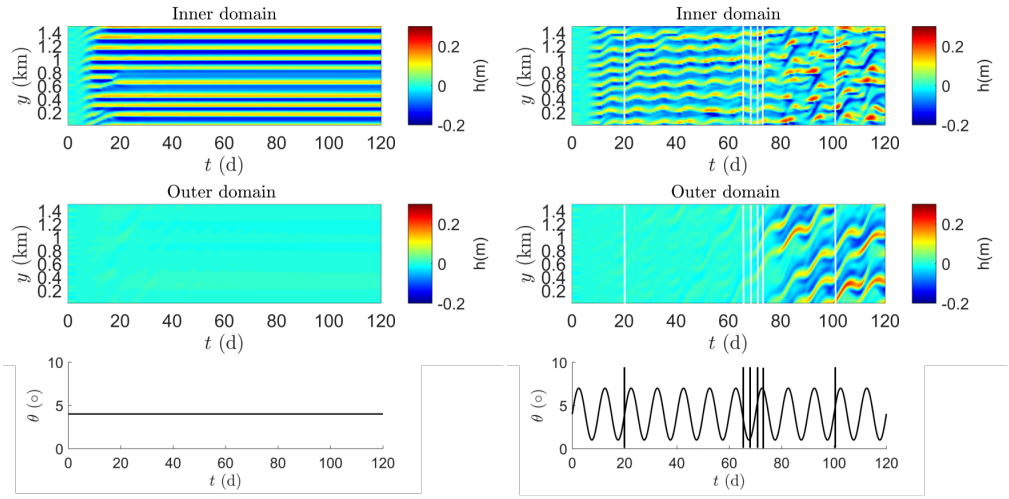

Figure 20: Left column: Run5 (constant wave forcing with $\theta_0^0 = 4^o$), right column: Run6T$_{10}$ (time-varying forcing with $\theta_0^0 = 4^o$, $A_\theta = 3^o$ and $T_\theta = 10$ days). The bottom perturbation along the longshore direction y in km is plotted as a function of time t in days. The section are taken at $x = 40$ m (inner bar) and at $x = 140$ m (outer bar), as indicated by the black lines in Figure 13. The angle of incidence at the offshore boundary is given below the longshore sections. The vertical lines in the longshore sections of in the right column and the plot of the angle indicate the moments for which the bottom perturbations in Figure 19 are shown.

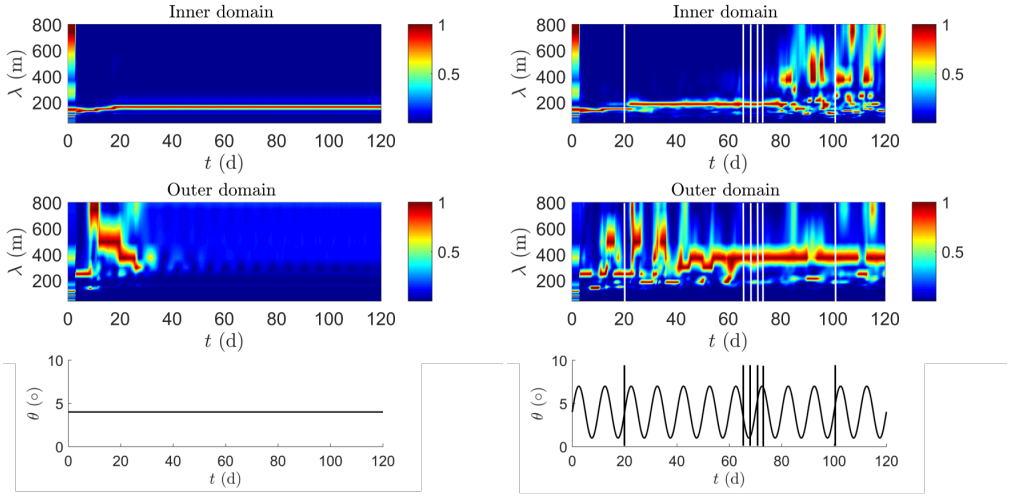

Figure 21: Time evolution of the scaled discrete power of the Fourier coefficients of $h(x, y, t)$ at x=40 m (inner domain) and x=40 m (outer domain), is shown for Run5 (constant wave forcing with $\theta_0^0 = 4^o$) in the left column and Run6T$_{10}$ (time-varying forcing with $\theta_0^0 = 4^o$, $A_\theta = 3^o$ and $T_\theta = 10$ days) in the right column. The vertical axis gives the dominant wavelength in meters as a function of the time t in days on the horizontal axis. The angle of incidence at the offshore boundary as a function of time is plotted below the panels showing the Fourier transformations. The vertical lines in the right column and the plot of the angle indicate the moments for which the bottom perturbations in Figure 19 are shown.

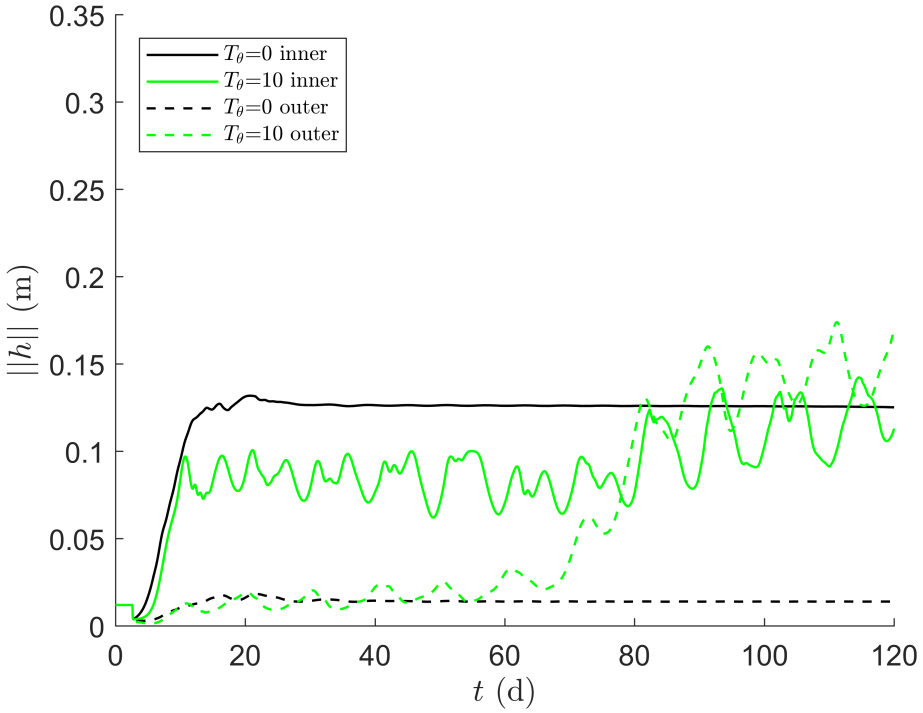

Figure 22: Root-mean square height of the bottom perturbation in meters as a function of the time in days. This is done for both the inner domain (solid line) and the outer domain (dashed line) for two different cases. The black line shows the results of the case with a period in wave angle of 0 days, so the wave angle is constant in time, Run5 ($\theta_0^0 = 4^o$, $T_\theta = 0$). The green line shows the results for the case with a period of 10 days in the wave angle, an amplitude $A_\theta = 3^o$ and a mean angle $\theta_0^0 = 4^o$, Run6T$_{10}$.

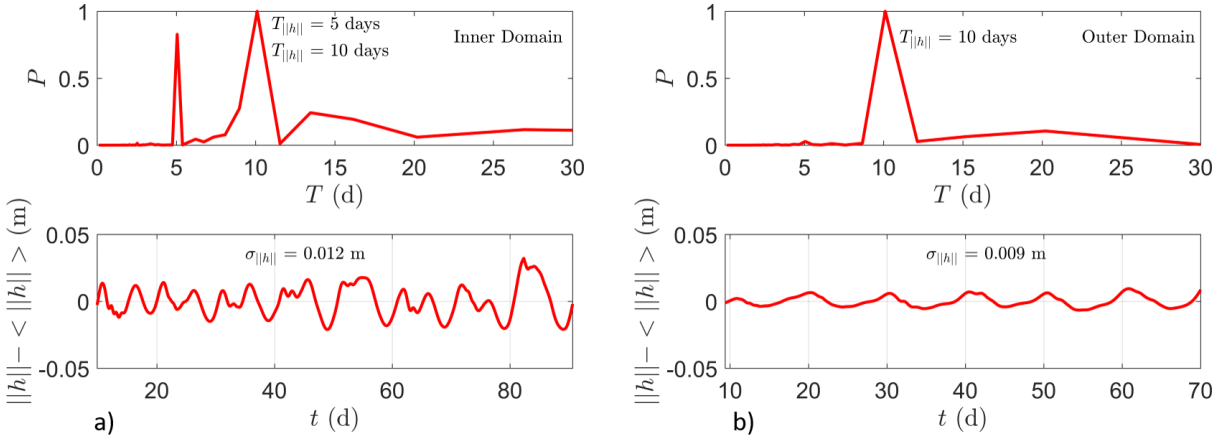

Figure 23: Upper panels: scaled discrete temporal power spectra of the function $||h||$ as shown in Figure 16 versus period (in days) for the inner domain (left) and outer domain (right), Run6T$_{10}$. Lower panels: time series of the residual root-mean square bar height with respect to its running mean ¡——h——¿.The standard deviation $\sigma_{||h||}$ (m) is calculated from this residual and shown in the plot.

4.2.2 Sensitivity to different forcing periods

In addition to the simulations evaluated above, Run6T has been done for period T_θ = 2.5, 5, 7.5, 10, 15, 20 and 25 days. These seven cases show a similar behaviour, initially bar form in the inner domain with a regular pattern. When the bars in the outer domain start to grow, the pattern in the inner domain becomes less regular.

This shift in regularity is seen clearly from Figure 33. After the bar in the outer domain have matured, the bars in the inner domain start to show larger deviations in h and the spacing between alternating bars becomes less regular (see also Figure 36). At this point, the bar pattern in the inner domain start to shift in the positive longshore direction but not as fast as the bars in the outer domain. The number of bars in the inner and outer domain is not influence by the period and is approximately the same in all cases.

The mean grow, $||h||_{av}(t)$ is smaller for time-varying angles than for a constant angle in all cases in the inner domain (see Appendix A Figures 35-37). In the outer domain, the bars do not grow for Run5 (constant angle), but do grow for time-varying angles (Run6T$_{10}$). When the bars in the outer domain start growing, the become larger than the bars in the inner domain.

The periods $T_{||h||}$ and standard deviation $\sigma_{||h||}$ for Run6T as a function of the forcing period T_θ are shown in Figure 24. For $10 \leq T_\theta \leq 20$ days, two dominant response periods were found in the inner domain. The response period in the inner domain show two linear correlations, $T_{||h||} = T_\theta$ and $T_{||h||} = \frac{1}{2}T_\theta$. The standard deviation of the fit through of $||h||$ shows an increase for an increasing period in the angle of the offshore waves. In the outer domain, only one dominant period was found for each T_θ namely $T_{||h||} = T_\theta$. The standard deviation shows again an increase for an increase in T_θ. In contrast to the cases with a normal mean wave angle, $\sigma_{||h||}$ does not show a peak around $T_\theta = 15$ days and seams only to increase.

4.2.3 Sensitivity to different forcing amplitudes

When looking at cases Run6T$_{10}$, Run7T$_{10}$ and Run8T$_{10}$ ($A_\theta = 3^o$, $A_\theta = 6^o$ and $A_\theta = 9^o$ respectively), all with an oblique mean angle, the influence of the amplitude can be analysed. The bar height in the inner domain decreases with an increase in the amplitude of the offshore wave angle (see Appendix A Figure 38).

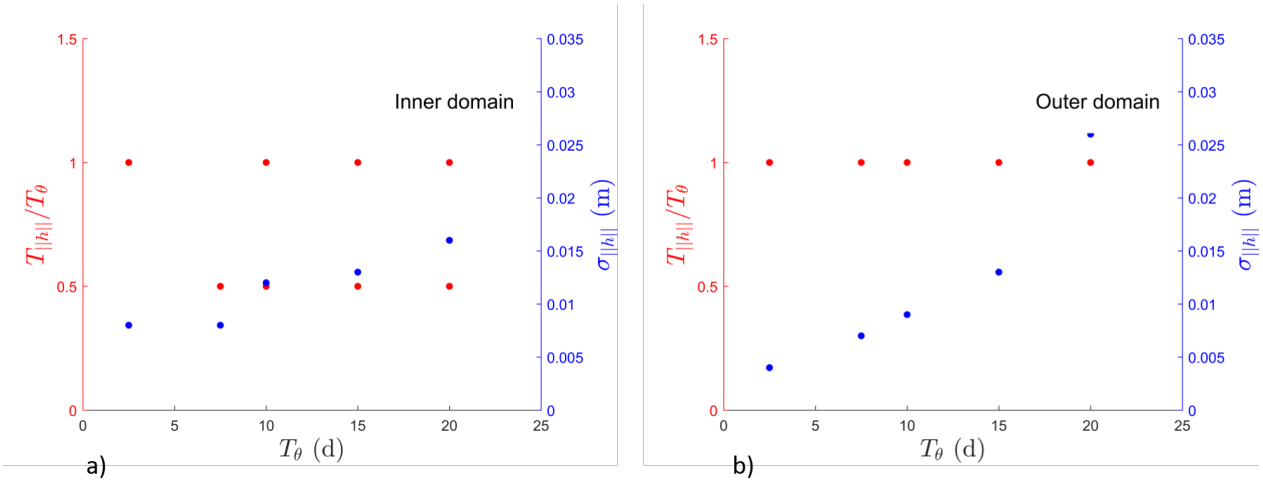

Figure 24: Dominant periods in the response $T_{||h||}$ scaled to the forcing period T_θ and the standard deviation $\sigma_{||h||}$ in meters of the root-mean square bar height $||h||$ on the left and right vertical axis respectively. The different forcing periods of wave angles T_θ (Run6T) for inner and outer domain are shown on the horizontal axis. The inner domain is shown in panel a) and the outer domain is shown in panel b). The evolution of Run6T$_5$ and Run6T$_{25}$ stopped to soon to get reliable information. In the inner domain, multiple dominant response periods were found for a single forcing period.

The bars for Run7T$_{10}$ and Run8T$_{10}$ show large amplitude differences and disappear almost entirely when the angle of incidence starts to decrease. This is also the moment that they show the largest displacement of approximately 1.5 bars in the longshore direction. When the angle of incidence increases, the bars start to grow again. There is no bar growth visible in the outer domain for Run7T$_{10}$ and Run8T$_{10}$.

The mean root-mean square perturbation $||h||_{av}(t)$ decreases for an increase in the amplitude A_θ for both the inner and outer domain (see Appendix A Figure 39). However, note that this difference is very small in the outer domain for $t < 70$ days.

For all three cases (Run6T$_{10}$, Run7T$_{10}$ and Run8T$_{10}$) the period $T_{||h||} = 10$ days, the same as the imposed period T_θ on the offshore boundary. The growth in the root-mean square bar height $||h||(t)$ in the inner is in phase with the growth in the outer domain for Run7T$_{10}$ and Run8T$_{10}$. For Run6T$_{10}$ the growth in the inner and outer domain is out of phase.

5 Discussion

5.1 Physical interpretation

5.1.1 Angle of incidence

The results of this thesis show a decrease in the growth of the bars for an increase in the wave angle. The cases with a normal mean wave angle no mature bars in the outer domain for the largest amplitude, $A_\theta = 9^o$. The cases with an oblique mean angle, the growth of the outer bars only happened for $A_\theta = 3^o$. Garnier et al. (2013) considered the influence of wave angle of incidence on the straightening of bars and investigated the physical mechanism behind the phenomena. An increase in the wave angle causes an increase in the longshore current and a decrease in the shoreward current. As a result, the intensity of the rip currents becomes weaker and less erosion takes place. On top of this, the position of the rip current is shifted downdrift, moving from the deepest section to a more shallow part. This shift is the drive behind a shift in position of the bars, but also prevents bars from forming or even straightening if the angles are large enough. The hydrodynamics of three different cases is shown in Figure 25 (Garnier et al. 2013). Showing the difference in direction of the total current, black arrows, and the cross-shore component, the grey scale. The ovals in all the panels are at the same position, the displacement of the rip currents, white areas, is evident from these results.

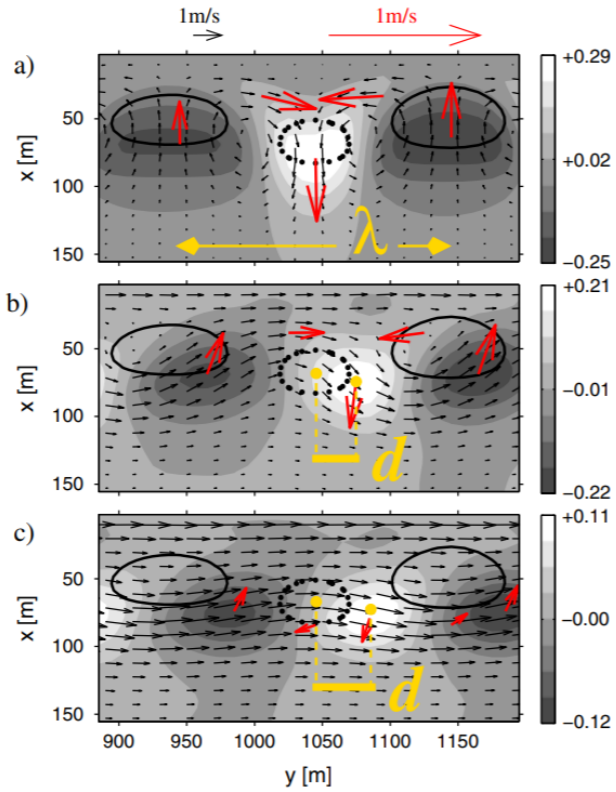

Figure 25: The hydrodynamics for a single-barred beach system for three different cases, a) $\theta^0 = 0^o$, b) $\theta^0 = 10^o$ and c) $\theta^0 = 20^o$. The vertical axis gives the cross-shore location with the coastal boundary is at $x = 0$. The horizontal axis gives part of the longshore domain, depicting 1/2 wavelength of the alongshore patterns in bar height. The solid and dotted line denote the horns and bays, respectively. The cross-shore velocity is indicated by the grey scale, with the white area offshore currents and the darkest areas the shoreward currents in m/s. Th total current is given by the black arrows, also in m/s. The residual current $(u, v - V)$ (with V the mean of v) is given by the red arrows. Figure from Garnier et al. (2013).

5.1.2 Coupling between inner and outer bars

Castelle et al. (2010) showed three different coupling types in their study. For low wave conditions, the bars displayed an in-phase coupling, for high wave conditions, the bars were out-of-phase and for intermediate conditions, the bars displayed a coupling at half the wavelength of the outer bar. The differences arise from the different processes that take place in the outer domain for different wave conditions. For intermediate wave conditions, the wave energy is to low for wave breaking to occur over the outer bars, only refraction of the waves takes places. Thus the waves keep most of their energy while the angle of the wave vector diminishes, increasing the magnitude of the cross-shore component of the wave vector. The result is a strong onshore flow over the inner bar that causes a net sediment loss in this area, and a horn on top of the longshore uniform outer bar facing a rip channel on the inner longshore uniform bar. This corresponds with our findings for the reference case, Run1, which displayed the twice as many bar in the alongshore direction on the inner bar than on the outer bar. The other cases, provided that there were matured bars in the outer domain, displayed similar behaviour. A bar on the outer bar faced a bay on the inner bar and the alongshore patterns were smaller in the inner domain than those in the outer domain, but not precisely twice as small.

For the cases with a larger amplitude or, the delay in growth of bars in the outer domain was largest. So the phase in the evolution of the system without bars in the outer domain, can best be studied from these cases. The bars in the inner domain were free to develop, independent of the outer domain. During this phase, the root-mean square bar height, $||h||(t)$, of the inner bars reached a quasi-equilibrium as expected based on the Castelle and Ruessink (2011). The moment the bars started to grow in the outer domain, they influenced the direction and strength of the wave that reached the inner bar. The inner bar was forced to adjust to the new wave conditions, merging and splitting occurred and $||h||(t)$ started to grow again. This one way coupling was not only found by Castelle et al. (2010), but later also by Thiebot et al. (2012) and Price et al. (2014).

The initial equilibrium of $||h||$ in the inner domain was disturbed by the growth of the bars in the outer domain and neither the inner bar nor the outer bar reached a equilibrium. Klein and Schuttelaars (2006) already investigated the stability of the non-linear behaviour of the double-barred beach system. Although the did not made the differentiation between $||h||$ in the inner and outer domain, they did find an initial exponential growth of the bars, followed by a phase of periodic $||h||$ with a growth in the mean value.

The delay in growth of the outer bar has been studied by Smit et al. (2008). They found a correlation between the volume of the bars and the delay in growth. Due to an decrease in volume, the active volume increased, i.e. the volume for which the breaker index $\gamma_b = H_s/D > 0.3$. This led to a decrease in the response time of the bars. In the present study, the outer uniform bar is higher and wider than the inner uniform bar and has thus a larger volume. The increase in response time of the outer bar can is thus in agreement with the findings of Smit et al. (2008).

5.1.3 Response of $||h||$, period and amplitude

The forcing of the change in angle of incidence is done sinusoidally. The change from the mean angle to its maximum, mean an minimum value respectively takes $\tau = \frac{1}{4}T_\theta$ days. The time of the system to adjust to a new angle of incidence t_a is called the response time of a system. When the response time is larger than the forcing period ($t_a > T_\theta$), inertia prevents the system to fully adjust to the new angle of incidence. As a result, the deviations in the mean value of $||h||$ will increase for an increase in the forcing period.

Nnafie et al. (2020) showed that for a single-barred beach system the maximum bar growth occurred for angles of $\theta^0_m = 1.5^o$ and 3^o. Similar results were found during the setup of this research, the mean bar growth reached a maximum for small angles. For time-varying wave angles, θ^o passes every angle between $\theta^0_0 \pm A_\theta$ twice during one forcing period T_θ. Depending on the mean wave angle, the domain for which waves have the largest growth ($-\theta^0_m \leq D_g \leq \theta^0_m$), is passed once or twice. This behaviour can explain the correlation between the forcing period T_θ and the response period $T_{||h||}$.

For normal mean angles, the wave angle passes the domain of maximum growth, D_g, twice during one forcing period, giving the system two boosts in growth. The response period $T_{||h||}$ is therefore expected to be $\frac{1}{2}T_\theta$.

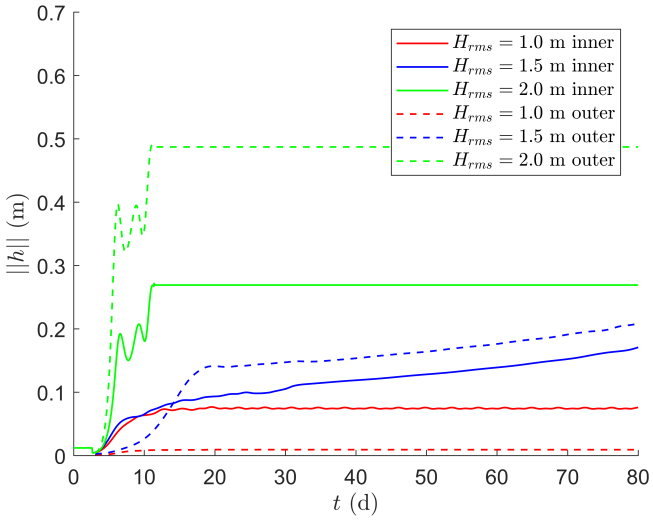

Figure 26: The root-mean square bar perturbations $||h||$ in meters are given as a function of the time in days. This is done for H_{rms} = 1, 1.5 and 2.0 m shown by the red lines, blue lines and the green lines respectively. Here, all wave conditions are taken constant, $\theta_0^0 = 0^o$ and wave period T = 9 s. At the point where the bar depth is 0.1 m, the simulations keeps the bar height constant. For H_{rms} = 2.0 m, the bars grow very fast and $||h||$ is kept constant.

For oblique mean angles, this boost can be different, depending on the forcing amplitude of the waves A_θ. For small amplitudes (A_θ θ_0^0), the bar height only has one large increases, θ^0 remains in the domain of maximum growth, displaying only one large boost in growth of the bar height $||h||(t)$. In this case, the response period will be the same as the forcing period, $T_{||h||} = T_\theta$. For larger angles, the bar height might have a large increase in bar growth twice during one forcing period. Because the mean angle is not normal to the coast, the time between these boosts will not be $\frac{1}{2}T_\theta$.

5.2 Choice for wave height

The wave height at the offshore boundary can be given as the root-mean square wave height, H_{rms}, or as the significant wave height, H_s. The latter is defined as the mean wave height of the largest third of all the waves. This value can be related to H_{rms} by $H_{rms} = \frac{1}{2}\sqrt{2}H_s$ (Holthuijsen 2007).

In this thesis, H_{rms} was constant at the offshore boundary and set to 1.5 meters. This is higher than the H_{rms} used by Price et al. (2013), H_{rms} = 0.78 m (H_s = 1.1 m), and Garnier et al. (2008) (H_{rms} = 1.0 m). Although the other parameters were mostly the same as either one of these articles, in this study, no activity was found on the outer bar for low values of H_{rms}. The difference between this study and the study done by Garnier et al. (2006) is that we examined a double-barred beach system, whereas Garnier et al. (2008) only considered single-barred beach systems. In the present study, activity was found in the inner domain for small wave heights, but not in the outer domain. Price et al. (2013) considered a double-barred systems, but they used a different model which might lead to different results for the same wave heights. The cross-shore profile was also slightly different, in the current study, the bar depth is larger. The choice made here is supported by Thiebot et al. (2012), who also studied a double-barred beach system with the model Morfo55. They chose H_{rms} = 1.5 m so that wave conditions would be energetic enough for instabilities to occur on both bars.

Figure 26 present the $||h||$ for three different cases with different H_{rms} at the offshore boundary. In this figure, $||h||$ in the inner and outer domain is indicated by the solid lines and the dashed lines respectively. This picture shows that the growth rate for H_{rms} = 2.0 m (green lines) is very high. This caused the bars to grow above the water level within the first 10 days. When the waves grew higher than 10 cm below the actual water level, the simulation stopped, this is the point were a constant bar height is given. For H_{rms} = 1.0 m

(the red lines) the inner bar went to equilibrium, but the outer bars did not show activity. The depth of the wave base was smaller than the depth D above the outer bar. For $H_{rms} = 1.5$ m (the blue lines) both the inner domain and the outer domain showed activity.

5.3 Model restrictions and advantages

There are some restrictions to the model used for this study, as mentioned by Garnier et al. (2006). Morfo55 does not account for feedback between the surf zone and the the swash zone or backshore. The coastline is modelled as a rigid boundary, thus erosion or accretion of the beach area is not taken into account. Migration of bars in the cross-shore direction has been observed by Rutten et al. (2019), amongst others, but is also not incorporated in this model. The bars are only allowed to grow and move in the longshore direction. Furthermore, the model only takes 2D processes into account and does not model 3D processes. This restriction is in particular of influence on the modelling of the undertow. Another restriction is given by the formulation of the wave model , which is highly simplified, only one frequency and wave direction are taken into account. Other models, like Morphodyn, often use the wave model SWAN, which does not have the same restrictions as the wave model incorporated in Morfo55. Morphodyn is used in some previously mentioned studies, Castelle et al. (2006), Castelle et al. (2010), and Price et al. (2013)

Morfo55 ends runs when a bar becomes higher than the actual sea level. This is a restriction that was of great influence on the present study. Because no equilibrium was reached in the bar root-mean square bar height, the bars kept growing and eventually reached the sea level. Simulations were therefore often stopped before the maximum time of 400 days they were supposed to run. A slight adjustment to the model was used to address this problem. The bar height was kept fixed when the depth above the bars became smaller than 0.1 m. The new bar height was calculated for every time step and if wanted to grow, it was kept fixed, if it became smaller, the fixed bar height was released. This allowed for the runs to continue longer than before.

An advantage of Morfo55 over Morphodyn, used by Castelle et al. (2010) and Price et al. (2013), is the the length of the domain. In the present study, the cross-shore domain is much smaller, 250 m, than the approximately 700 m used by Price et al. (2013). Their domain was chosen this large because model needed time to adjust to the wave conditions before waves were forced over bars in the nearshore region. Morfo55 does not have this limitation, so the domain can be smaller, effectively decreasing the time it takes for a simulation the be run.

5.4 Suggestions for further research

The results of this study give a better understanding about the coupling between the inner and outer bars as well as the response of $||h||$ to an increase in forcing period, T_θ and the amplitude of the wave angle, A_θ. But to achieve a better understanding of the coupling between T_θ and the response period of $||h||$, $T_{||h||}$, a study of the response time, $t_{||h||}$, of the double-barred beach system to a change in angle would be interesting as this would allow for a quantification of the explanation in subsection 5.1. It would also be interesting to do a follow up study on the influence of a sinusoidally varying wave height for different constant angles with

$$H^0_{rms} = A_H \sin(\frac{2\pi t}{T_H}) + H^0_{rms,0}.$$

The same analyses as the current study can be used to investigate the influence of the period T_H and amplitude A_H of these variations.

One could also try to modify the model such that it can deal with bar heights that reach the sea level. This might be done by improving the model for this specific situation, however changing the position of the inner bar might also help. The position was taken to be at the same location as in the study of Price et al. (2013), which corresponds to observations done on the Gold Coast in Australia. However, when the location of the inner uniform bar is shifted in the cross-shore direction away from the coast, the depth becomes larger and simulations might continue longer.

6 Conclusions

In order to answer the research question of this study: *What is the response of a double-barred beach system to periodically time-varying wave angles?*, a case with time-varying wave angles has been compared to a reference case where constant wave conditions were imposed. Three subquestions have been investigated to investigate the influence of different time-varying conditions: *What is the influence of the forcing period of the angles?; What is the influence of the maximum amplitude of the variations in the angle?; What is the influence of the mean angle?.*

In the case with constant wave forcing and a normal mean wave angle, $\theta_0^0 = 0^o$, the inner and outer bar showed a coupling at half the wavelength of the outer domain (as defined in Section 5.1.2). The reference case with oblique mean angles, $\theta_0^0 = 4^o$ showed no bar growth in the outer domain, only for time-varying angles did the bars in the outer domain grow. For time-varying wave angles, the coupling between the inner and outer bar was less pronounced, but it resembled a coupling at half the wave length of the outer domain with a horn on the outer bar facing a bay on the inner bar. Both references cases had a total bar growth in the inner domain larger than for time-varying wave angles. In the outer domain, there were only matured bars for normal mean angles. The total bar growth of this case was approximately the same as for time-varying angles.

For an increase in the forcing period of the wave angles, T_θ, the response period of the root-mean square bar height, $T_{||h||}$ increased. This response was the same in the inner and outer domain for the normal mean wave angle, $T_{||h||} = \frac{1}{2}T_\theta$. For the cases with $\theta_0^0 = 4^o$, the inner domain showed two dominant response periods, $T_{||h||} = \frac{1}{2}T_\theta$ and T_θ. The outer domain showed only one response period of $T_{||h||} = T_\theta$. An increase in T_θ also corresponded with an increase in the standard deviation of $||h||(t) - ||h||_{av}(t)$, $\sigma_{||h||}$. For normal mean incidence, the increase in $\sigma_{||h||}$ had a maximum at $T_\theta = 15$ days. This maximum did not occur for oblique waves, in those cases, $\sigma_{||h||}$ kept increasing for increasing T_θ.

The amplitude of the angle of incidence was increased from 3^o to 6^o to 9^o. The increase in the amplitude caused a decrease in the total bar growth in both the inner and outer domain and an increase in the response time, $t_{||h||}$, of the outer bar. When bars in the outer domain started to mature, the patterns in the inner domain started to change and became less regular. For the cases with an oblique mean angle and amplitudes $A_\theta \geq 6^o$, no matured bars were found in the outer domain, only in the inner domain. No correlation was found between an increase in the amplitude of the wave angle and the response period $T_{||h||}$ or the standard deviation $\sigma_{||h||}$. The conclusions are summarized in Table 6.

The influence of the oblique mean wave angles was mainly the same as the increase of the amplitude of the wave angles. The response time of the bar in the outer domain increased and for some cases, no bars formed during the 120 days of the simulations. Another effect of the oblique mean angle was the shift in longshore position of the bars. The bars had a net downshift movement in both the inner and outer domain.

	Reference case		Increase T_θ		Increase A_θ	
Case	matured bars	$\|\|h\|\|_{av}$	$T_{\|\|h\|\|}$	$\sigma_{\|\|h\|\|}$	$\|\|h\|\|_{av}$	$t_{\|\|h\|\|}$
NI	yes	$\|\|h\|\|_{rc} > \|\|h\|\|_{tv}$	$T_{\|\|h\|\|} = \frac{1}{2}T_\theta$	max for $T_\theta = 15$ days	decreases	unchanged
NO	yes	$\|\|h\|\|_{rc} \approx \|\|h\|\|_{tv}$	$T_{\|\|h\|\|} = \frac{1}{2}T_\theta$	max for $T_\theta = 15$ days	decreases	increases
OI	yes	$\|\|h\|\|_{rc} > \|\|h\|\|_{tv}$	$T_{\|\|h\|\|} = \frac{1}{2}T_\theta$, T_θ	continues increase	decreases	unchanged
OO	no	$\|\|h\|\|_{rc} < \|\|h\|\|_{tv}$	$T_{\|\|h\|\|} = T_\theta$	continues increase	decreases	increases

Table 6: The conclusions normal wave incidence in the inner domain (NI) and outer domain (NO), oblique wave incidence in the inner domain (OI) and outer domain (OO). The response of the system for the reference cases, an increase in the forcing period, T_θ, and an increase in the amplitude of the angle, A_θ, are given. Here, $||h||_{av}$ is the average bar height and $||h||_{rc}$ is the mean bar height for the reference cases, $||h||_{tv}$ is the mean bar height for time-varying wave angles. Furthermore, $T_{||h||}$ is the response period of $||h||(t)$, $\sigma_{||h||}$ is the standard deviation of $||h||$ with respect to $|h||_{av}$ and $t_|h||$ is the response time of the bars.

Acknowledgement

I would like to thank my supervisors Prof. Dr. Huib de Swart, Dr. Abdel Nnafie and Dr. Timothy Price for their guidance in the process of writing this thesis. They have been there every step along the way providing advice and encouragement.
I especially want to thank Huib de Swart by stimulating my enthusiasm for the subject. It was his enthusiasm during lectures and presentations that made me choose to do research to the dynamics of coastal areas. Additionally, his never ending positive attitude during meetings and constructive criticism helped me to create the best result I was able to achieve.
Lastly, I also would like to thank Abdel Nnafie for all the adjustments and improvements he has made to the model. He also offered great support in the field of programming so that the data could be represented in a clear manner.

References

Almar, R., B. Castelle, G. Ruessink, N. Senechal, P. Bonneton, and V. Marieu (2010). "Two- and three-dimensional double-sandbar system behaviour under intense wave forcing and a meso–macro tidal range". In: *Continental Shelf Research* 30, pp. 781–792. DOI: 10.1016/j.csr.2010.02.001.

Bashforth, F. and J. Adams (1883). *An Attempt to Test the Theories of Capillary Action by Comparing the Theoretical and Measured Forms of Drops of Liquids with an Explanation of the Method of Integration Employed in Constructing the Tables Which Give the Theoretical Forms of Such Drops*. Cambridge University Press.

Battjes, J. A. (1975). "Modeling of turbulence in the surf zone". In: *Proc. Symp. Modeling tech.* Vol. 2. A.S.C.E., San Francisco, U.S.A., pp. 2050–1061.

Brander, R., D. Dominey-Howes, C. Champion, O. Vecchio, and B. Brighton (2013). "Brief Communication: A new perspective on the Australian rip current hazard". In: *Natural Hazards and Earth System Science* 13, pp. 1687–1690. DOI: 10.5194/nhess-13-1687-2013.

Caballeria, M., G. Coco, A. Falques, and D. A. Huntley (2002). "Self-organization mechanisms for the formation of nearshore crescentic and transverse bars". In: *Journal of Fluid Mechanics* 465, pp. 379–410. DOI: 10.1017/S002211200200112X.

Castelle, B., P. Bonneton, and R. Butel (2006). "Modélisation du festonnage des barres sableuses d'avant-côte : application à la côte aquitaine, France". In: *Comptes Rendus Geosciences* 338. DOI: 10.1016/j.crte.2006.06.007.

Castelle, B., P. Bonneton, H. Dupuis, and N. Senechal (2007). "Double bar beach dynamics on the high-energy meso-macrotidal French Aquitanian Coast: A review". In: *Marine Geology* 245, pp. 141–159. DOI: 10.1016/j.margeo.2007.06.001.

Castelle, B. and G. Ruessink (2011). "Modeling formation and subsequent nonlinear evolution of rip channels: Time-varying versus time-invariant wave forcing". In: *Journal of Geophysical Research* 116. DOI: 10.1029/2011JF001997.

Castelle, B., G. Ruessink, P. Bonneton, V. Marieu, N. Bruneau, and T. Price (2010). "Coupling mechanisms in double sandbar systems. Part 1: Patterns and physical explanation". In: *Earth Surface Processes and Landforms* 35, pp. 476–486. DOI: 10.1002/esp.1929.

Coco, G., D. Calvete Manrique, F. Ribas, H. de Swart, and A. Falques (2020). "Emerging crescentic patterns in modelled double sandbar systems under normally incident waves". In: *Earth Surface Dynamics* 8, pp. 323–334. DOI: 10.5194/esurf-8-323-2020.

Davis Jr., R.A. and D. M. Fitzgerald (2004). *Beaches and Coasts*. Blackwell Science Ltd, Malden U. S. A.

Garnier, R., D. Calvete, A. Falques, and M. Caballeria (2006). "Generation and nonlinear evolution of shore-oblique and transverse sand bars". In: *Journal of Fluid Mechanics* 567, pp. 327–360. DOI: 10.1017/S0022112006002126.

Garnier, R., D. Calvete, A. Falques, and N. Dodd (2008). "Modelling the formation and the long-term behavior of rip channel systems from the deformation of a longshore bar". In: *Journal of Geophysical Research* 113. DOI: 10.1029/2007JC004632.

Garnier, R., A. Falques, D. Calvete Manrique, J. Thiebot, and F. Ribas (2013). "A mechanism for sandbar straightening by oblique wave incidence". In: *Geophysical Research Letters* 40, pp. 2726–2730. DOI: 10.1002/grl.50464.

Gensini, Vittorio and Walker Ashley (2010). "An examination of rip current fatalities in the United States". In: *Natural Hazards* 54, pp. 159–175. DOI: 10.1007/s11069-009-9458-0.

Gleick, P. H. (1993). *Water in Crisis: A Guide to the World's Fresh Water Resources*. Oxford University Press, New York).

Groen, P. and R. Dorrestein (1976). *Zeegolven*. 3rd. Staatsdrukkerij- en uitgeverijbedrijf 's-Gravenhage, the Netherlands.

Haslett, S. K. (2000). *Coastal Systems*. 3rd. University of Wales Press, Cardiff, U. K.

Holthuijsen, L.H. (2007). *Waves in Oceanic and Coastal Waters*. Cambridge University Press. ISBN: 9781139462525.

Horikawa, K. (1988). *Nearshore Dynamics and Coastal Processes*. University of Tokyo Press, Japan.

King, C. A. M. and W. W. Williams (2020). "The formation and movement of sand bars by wave action". In: *Geographical Journal* 113, pp. 70–85. DOI: 10.2307/1788907.

Klein, M. and H. M. Schuttelaars (2006). "Morphodynamic evolution of double-barred beaches". In: *Journal of Geophysical Research* 111. DOI: 10.1029/2005JC003155.

Lippmann, T. and R. Holman (1990). "The spatial and temporal variability of sand bar". In: *Journal of Geophysical Research* 95. DOI: 10.1029/JC095iC07p11575.

Longuet-Higgins, M. S. and R. W. Stewart (1964). "Radiation stresses in water waves: A physical discussion, with applications". In: *Deep Sea Research and Oceanographic Abstracts* 11, pp. 529–562. DOI: 10.1016/0011-7471(64)90001-4.

Luijendijk, A., G. Hagenaars, R. Ranasinghe, F. Baart, G. Donchyts, and S. Aarninkhof (2018). "The State of the World's Beaches". In: *Scientific Reports* 8. DOI: 10.1038/s41598-018-24630-6.

Marshak, S. (1955). *Earth, Portrait of a Planet*. 5th. W. W. Norton and Company, New York, U. S. A.

Mei, C. C. (1989). *The Applied Dynamics of Ocean Surface Waves, Advanced Series on Ocean Engineering*. Worl Scientific, Singapore.

Nnafie, A., N. Van Andel, and H. De Swart (2020). "Modelling the impact of a time-varying wave angle on the nonlinear evolution of sand bars in the surf zone". In: *Earth Surface Processes and Landforms*. DOI: 10.1002/esp.4916.

Price, T., B. Castelle, R. Ranasinghe, and G. Ruessink (2013). "Coupled sandbar patterns and obliquely incident waves". In: *Journal of Geophysical Research: Earth Surface* 118. DOI: 10.1002/jgrf.20103.

Price, T., G. Ruessink, and B. Castelle (2014). "Morphological coupling in multiple sandbar systems – a review". In: *Earth Surface Dynamics* 2, pp. 309–321. DOI: 10.5194/esurf-2-309-2014.

Ribas, F., A. Falques, H. De Swart, N. Dodd, R. Garnier, and D. Calvete Manrique (2015). "Understanding coastal morphodynamic patterns from depth-averaged sediment concentration". In: *Reviews of Geophysics* 53. DOI: 10.1002/2014RG000457.

Ruessink, G., G. Coco, R. Ranasinghe, and I. Turner (2007). "Coupled and noncoupled behavior in double sandbar morphology". In: *Journal of Geophysical Research* 112. DOI: 10.1029/2006JC003799.

Rutten, J., B. Dubarbier, T. D. Price, G. Ruessink, and B. Castelle (2019). "Alongshore Variability in Crescentic Sandbar Patterns at a Strongly Curved Coast". In: *Journal of Geophysical Research: Earth Surface* 124. DOI: 10.1029/2019JF005041.

Short, A. and C. Woodroffe (2009). *The Coast of Australia*. Cambridge University Press, Melbourne. ISBN: 9780521873987.

Smit, M. W. J., A. J. H. M. Reniers, B. G. Ruessink, and J. A. Roelvink (2008). "The morphological response of a nearshore double sandbar system to constant wave forcing". In: *Coastal Engineering* 55.10, pp. 761–770. DOI: 10.1016/j.coastaleng.2008.02.010.

Soulsby, R. L. (1997). *Dynamics of Marine Sands*. Thomas Telford, London.

Stive, M. J. F., M. A. De Schipper, A. P. Luijendijk, S. G. J. Aarninkhof, C. Van Gelder-Maas, J. S. M. Van Thiel de Vries, S. De Vries, M. Henriquez, S. Marx, and R. Ranasinghe (2013). "A New Alternative to Saving Our Beaches from Sea-Level Rise: The Sand Engine". In: *Journal of Coastal Research* 29, pp. 1001–1008. DOI: 10.2112/JCOASTRES-D-13-00070.1.

Thiebot, J., D. Idier, R. Garnier, A. Falques, and G. Ruessink (2012). "The influence of wave direction on the morphological response of a double sandbar system". In: *Continental Shelf Research* 32, pp. 71–85. DOI: 10.1016/j.csr.2011.10.014.

Thornton, E. and R. Guza (1983). "Transformation of wave height distribution". In: *Journal of Geophysical Research* 88, pp. 5925–5938. DOI: 10.1029/JC088iC10p05925.

Van Enckevort, I. M. J., B. G. Ruessink, G. Coco, K. Suzuki, I. L. Turner, N. G. Plant, and R. A. Holman (2004). "Observations of nearshore crescentic sandbars". In: *Journal of Geophysical Research* 109. DOI: 10.1029/2003JC002214.

Wright, L. D. and A. D. Short (1984). "Morphodynamics variability of surf zones and beaches: A synthesis". In: *Marine Geology* 70, pp. 251–285.

Yu, J. and D. Slinn (2003). "Effects of wave-current interaction on rip currents". In: *Journal of Geophysical Research* 108. DOI: 10.1029/2001JC001105.

A Figures

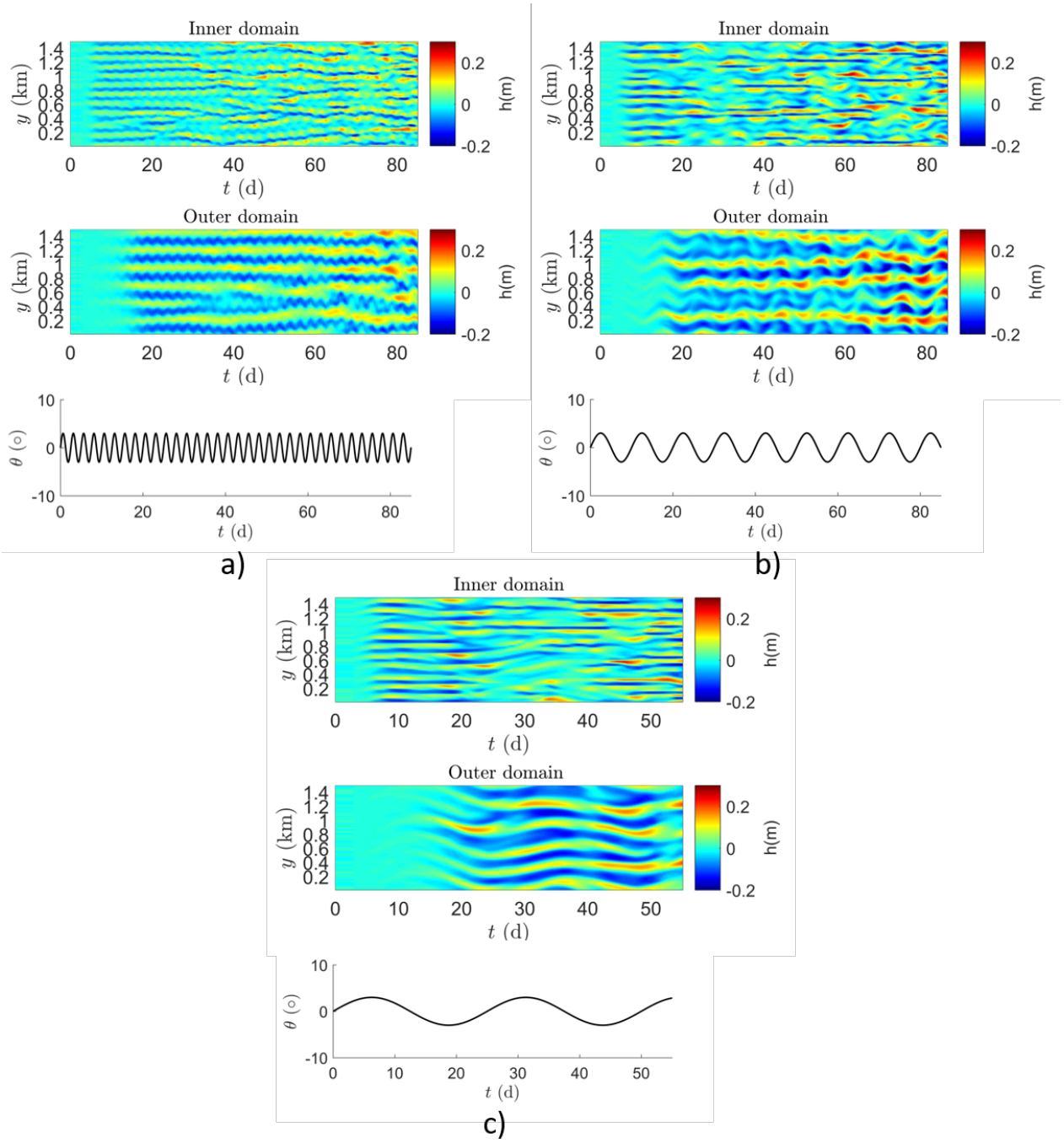

Figure 27: The longshore sections of a) Run2T$_{2.5}$ ($A_\theta = 3^o$, $T_\theta = 2.5$ days), b) Run2T$_{10}$ ($A_\theta = 3^o$, $T_\theta = 10$ days) and c) Run2T$_{25}$ ($A_\theta = 3^o$, $T_\theta = 25$ days. The longshore direction in km is given on the vertical axis and time t in days is given on the horizontal axis. The perturbations on top of the uniform bars is given by the colours with blue the deepened areas, so erosion takes place, and red areas that became more shallow, so net sedimentation takes place. The angle of incidence in degrees at the offshore boundary as a function of time is also plotted for all cases.

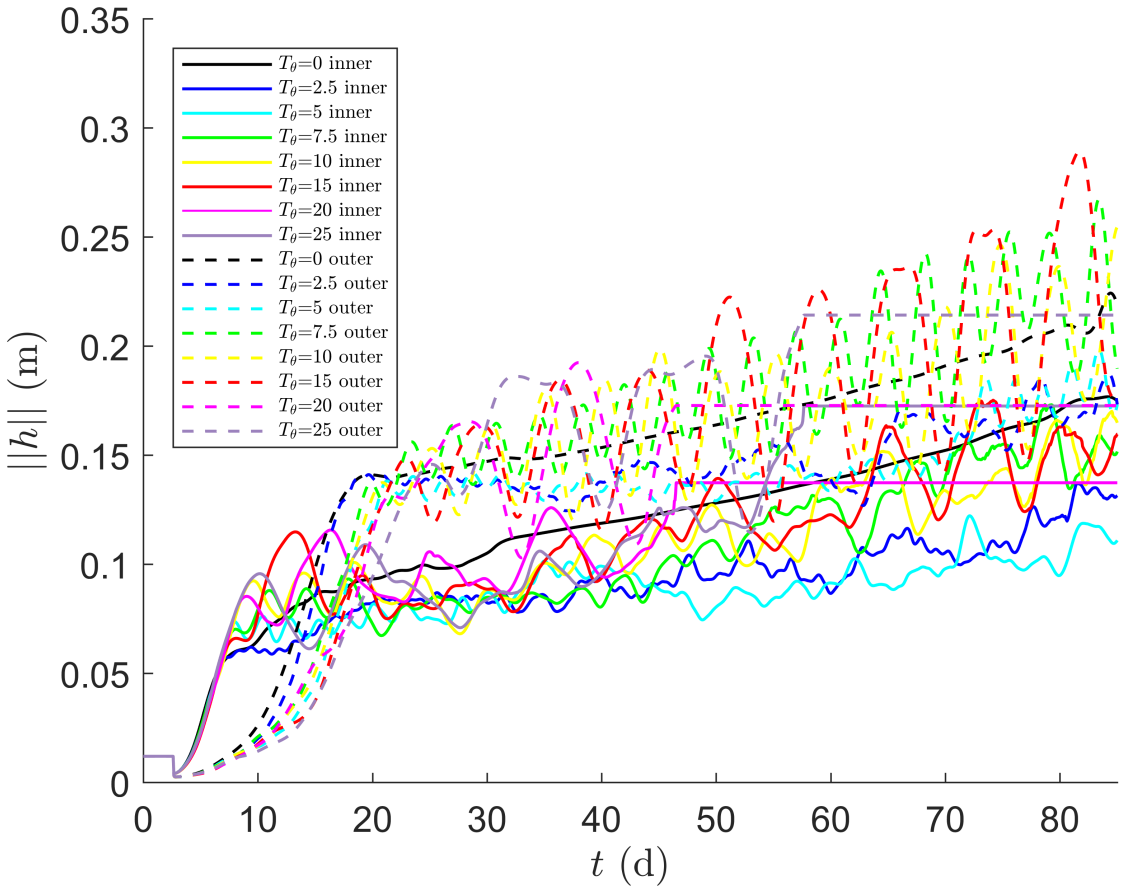

Figure 28: This figure shows the root-mean square bottom perturbation $||h||$ in meters as a function of the time in days. This is done for both the inner domain (solid line) and the outer domain (dashed line) for cases Run1, the black lines and Run2T, the coloured lines.

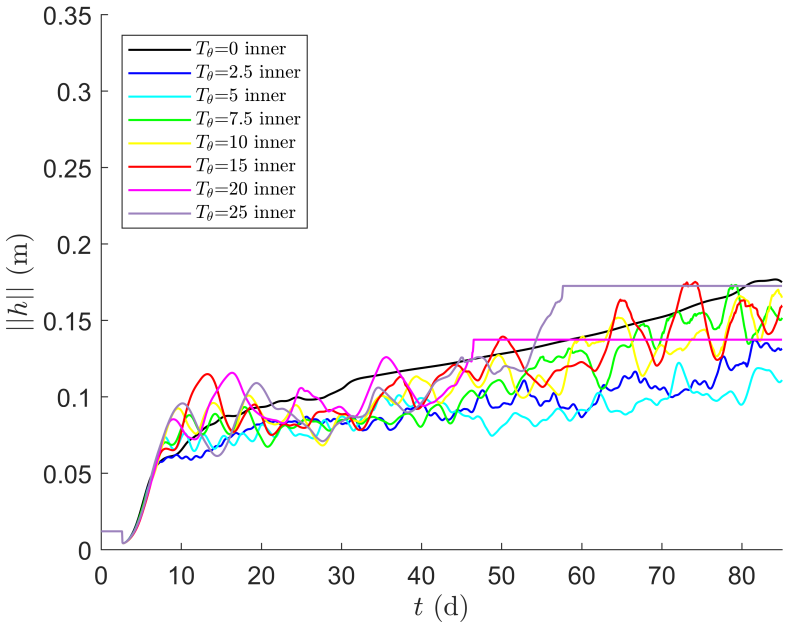

Figure 29: This figure shows the root-mean square bottom perturbation $||h||$ in meters as a function of the time in days. This is done for both the inner domain for cases Run1, the black lines and Run2T, the coloured lines.

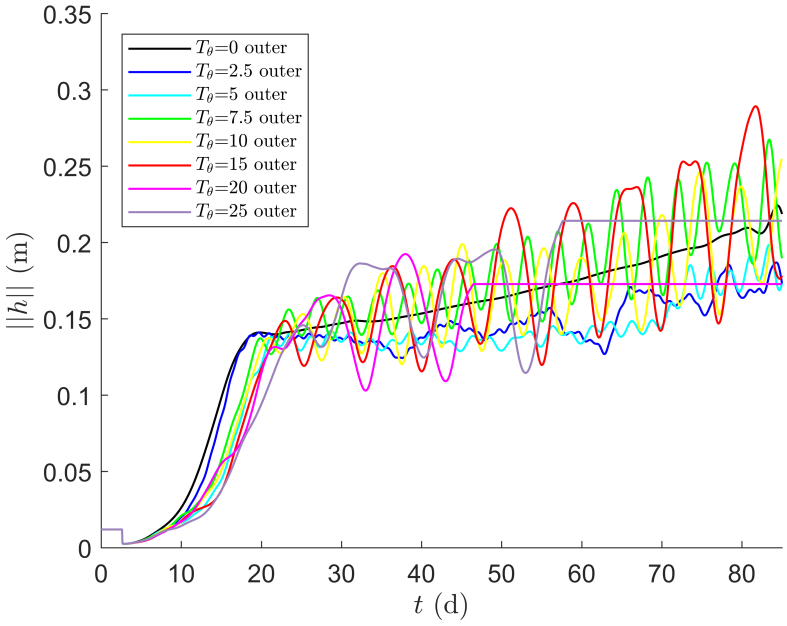

Figure 30: This figure shows the root-mean square bottom perturbation $||h||$ in meters as a function of the time in days. This is done for both the outer domain for cases Run1, the black lines and Run2T, the coloured lines.

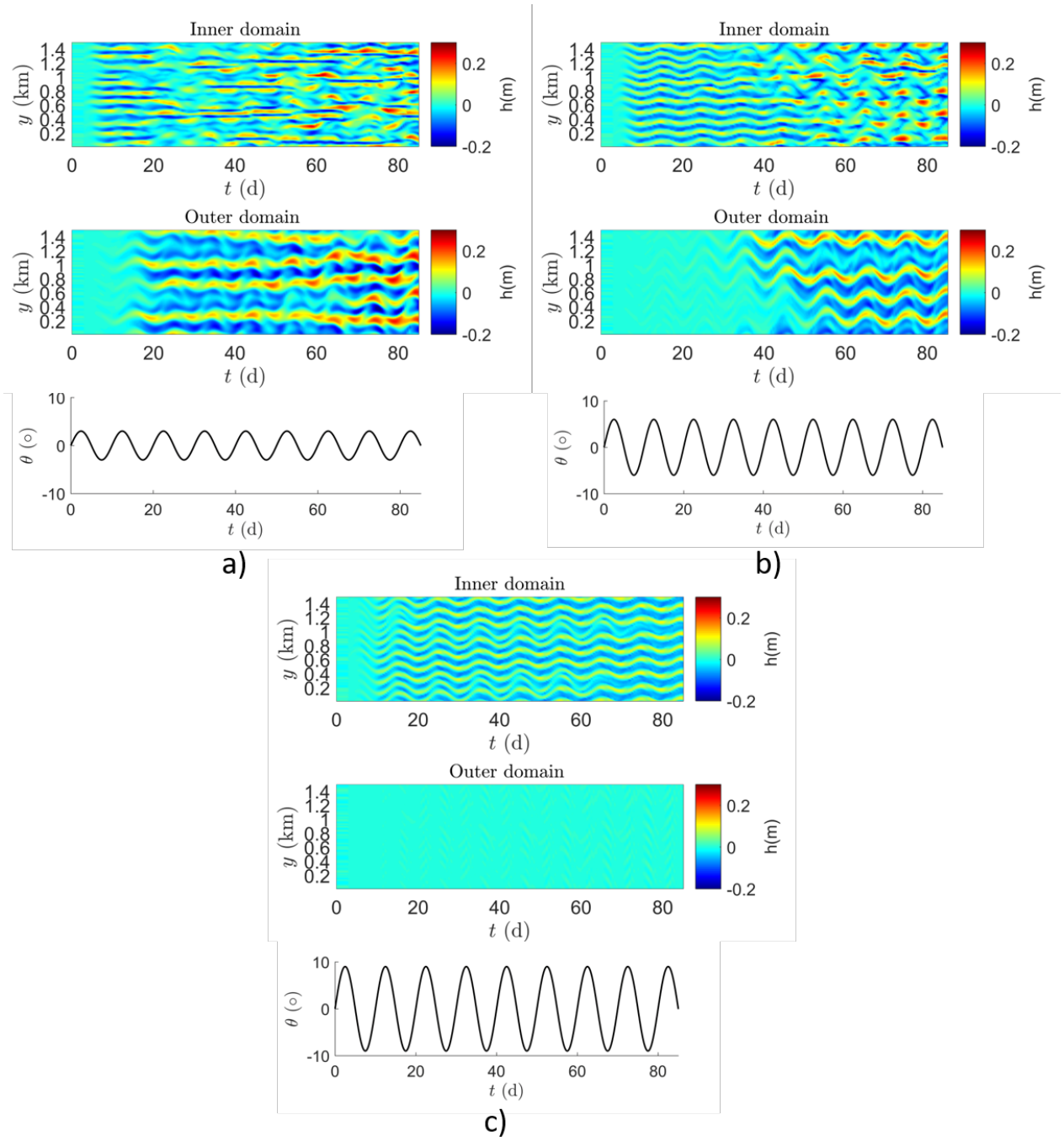

Figure 31: The longshore sections of a) Run2T$_{10}$ ($A_\theta = 3^o$, $T_\theta = 10$ days), b) Run3T$_{10}$ ($A_\theta = 6^o$, $T_\theta = 10$ days) and c) Run4T$_{10}$ ($A_\theta = 9^o$, $T_\theta = 10$ days. The longshore direction in km is given on the vertical axis and time t in days is given on the horizontal axis. The perturbations on top of the uniform bars is given by the colours with blue the deepened areas, so erosion takes place, and red areas that became more shallow, so net sedimentation takes place. The angle of incidence in degrees at the offshore boundary as a function of time is also plotted for all cases.

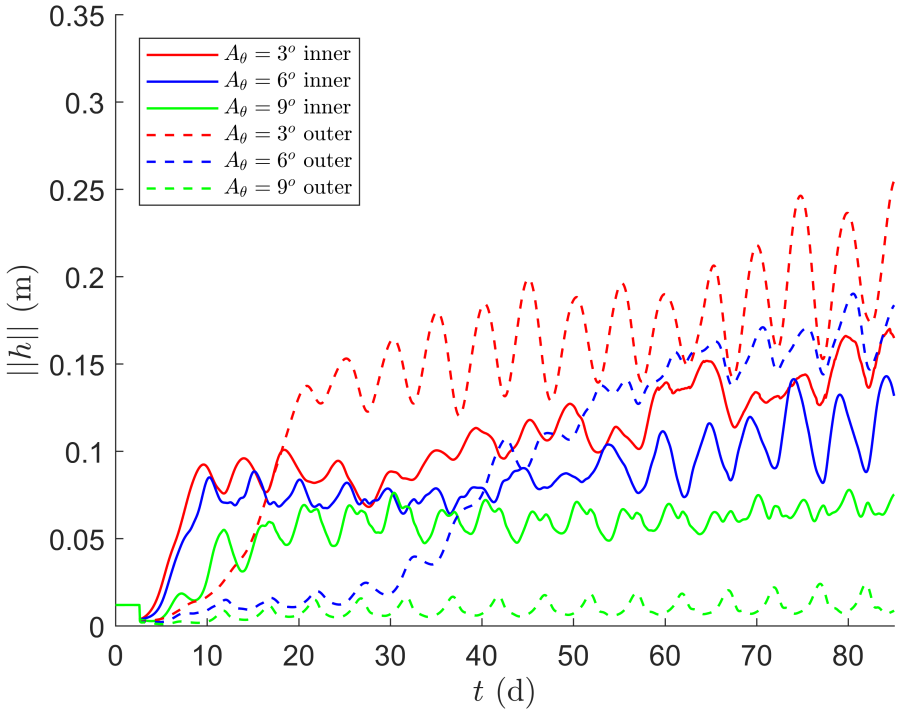

Figure 32: The root-mean square bar height $||h||(t)$ in meters as a function of time in days is given for Run2T_{10}, Run3T_{10} and Run4T_{10} as the red line, the blue line and the green line respectively. With the inner domain indicated by the solid line and the outer domain with the dashed line. This shows the influence of the amplitude of the of the wave angle at the offshore boundary at the mean growth rate ate the two domains.

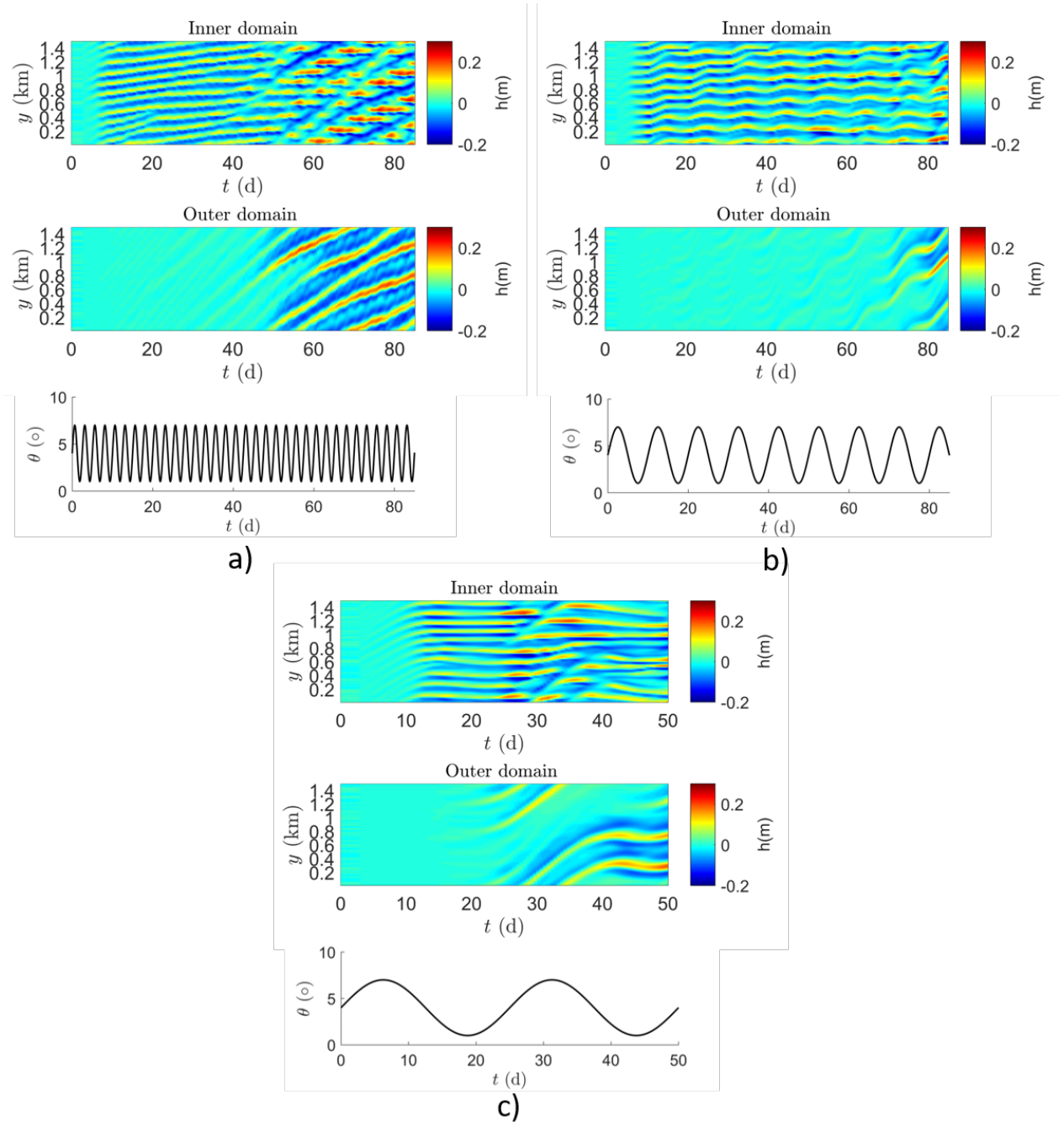

Figure 33: The longshore sections of a) Run6T$_{2.5}$ ($\theta_0^0 = 4^o$, $A_\theta = 3^o$ and $T_\theta = 2.5$ days), b) Run6T$_{10}$ ($\theta_0^0 = 4^o$, $A_\theta = 3^o$ and $T_\theta = 10$ days) and c) Run6T$_{25}$ ($\theta_0^0 = 4^o$, $A_\theta = 3^o$, $T_\theta = 25$ days. The longshore direction in km is given on the vertical axis and time t in days is given on the horizontal axis. The perturbations on top of the uniform bars is given by the colours with blue the deepened areas, so erosion takes place, and red areas that became more shallow, so net sedimentation takes place. The angle of incidence in degrees at the offshore boundary as a function of time is also plotted for all cases.

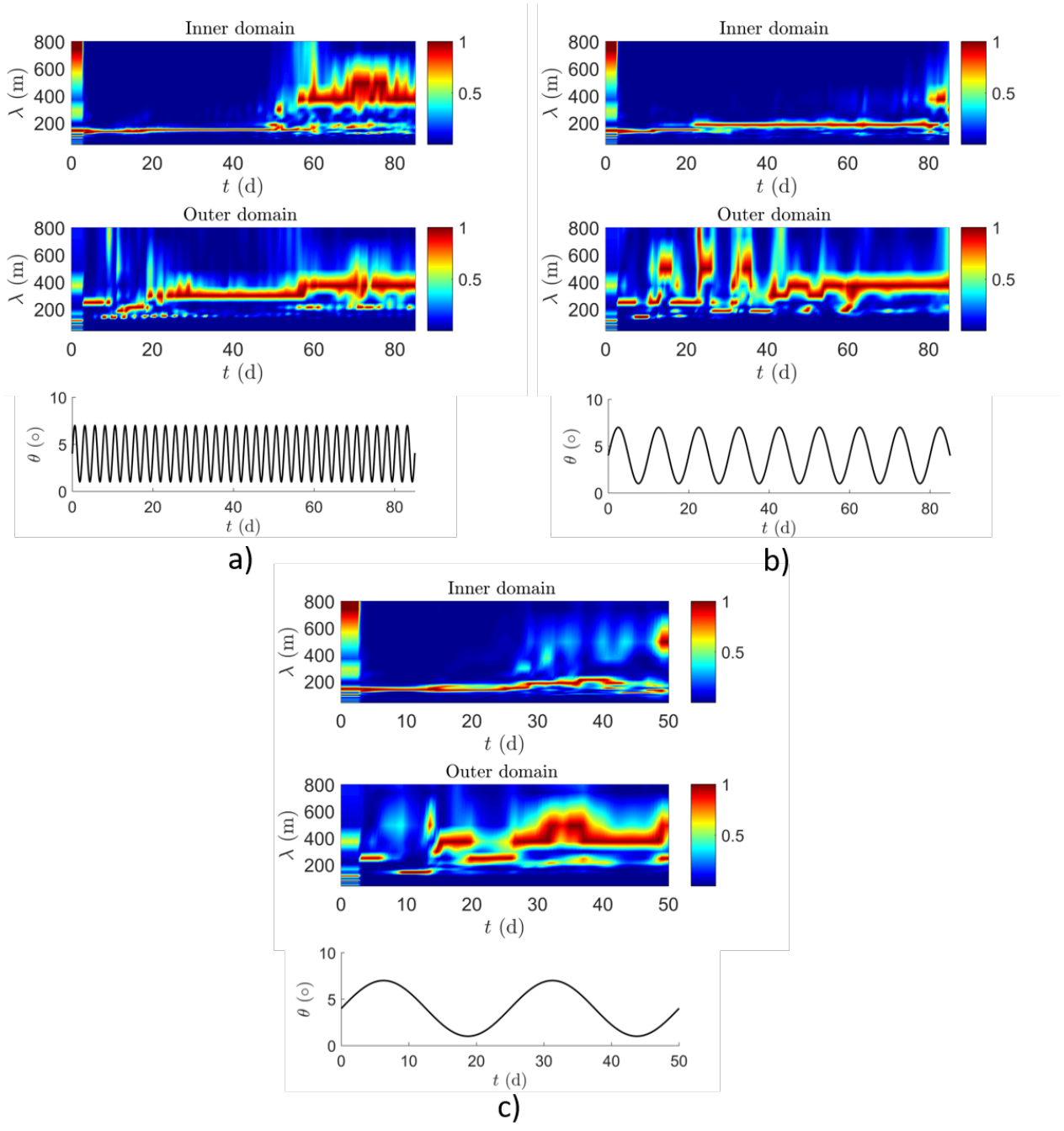

Figure 34: Time evolution of the scaled discrete power of the Fourier coefficients of $h(x, y, t)$ at x=40 m (inner domain) and x=40 m (outer domain), is shown for a) Run5T$_{2.5}$ b) Run5T$_{10}$ c) Run5T$_{25}$. The vertical axis gives the dominant wavelength in meters as a function of the time t in days on the horizontal axis

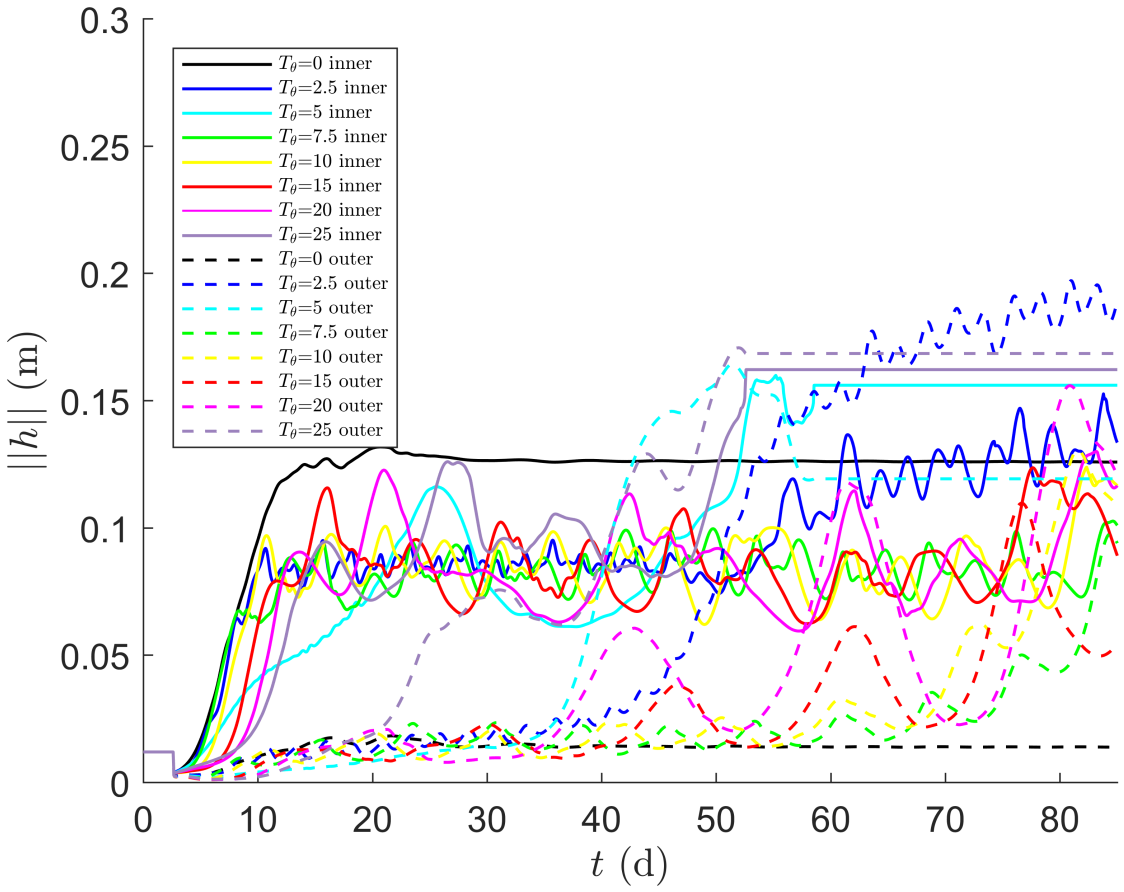

Figure 35: This figure shows the root-mean square bottom perturbation $||h||$ in meters as a function of the time in days. This is done for both the inner domain (solid line) and the outer domain (dashed line) for cases Run5, the black lines and Run6T, the coloured lines.

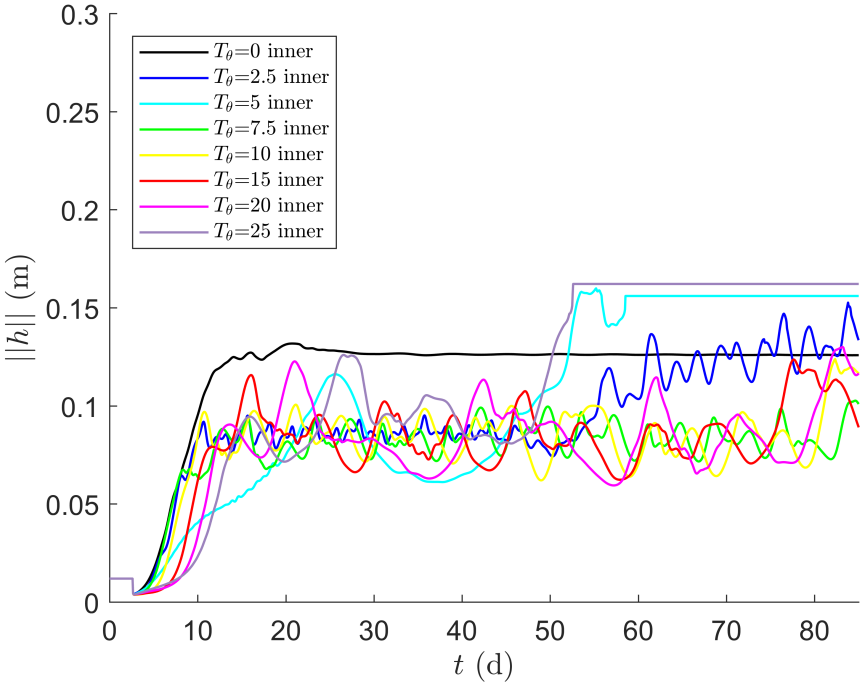

Figure 36: This figure shows the root-mean square bottom perturbation $||h||$ in meters as a function of the time in days. This is done for both the inner domain for cases Run5, the black lines and Run6T, the coloured lines.

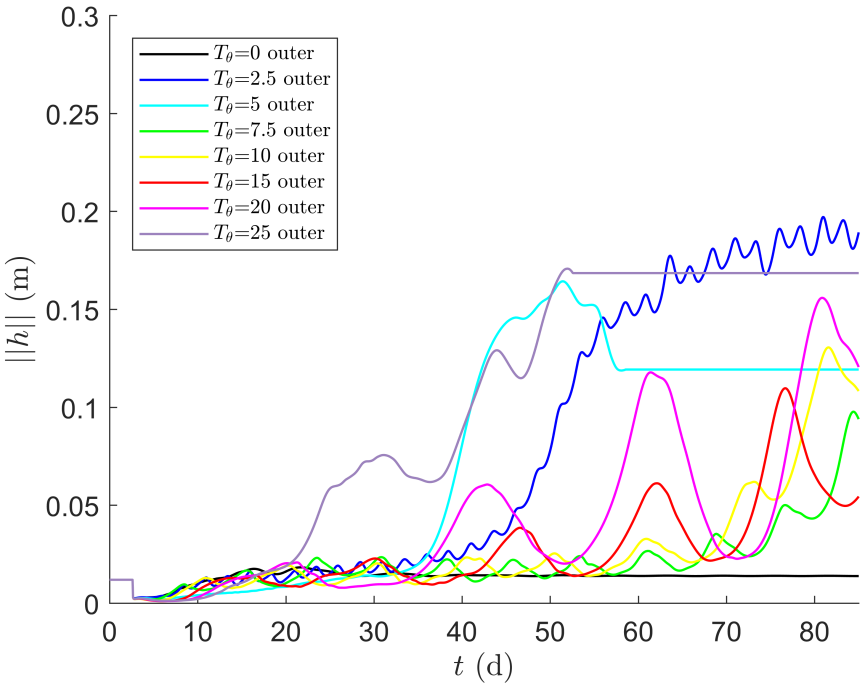

Figure 37: This figure shows the root-mean square bottom perturbation $||h||$ in meters as a function of the time in days. This is done for both the outer domain for cases Run5, the black lines and Run6T, the coloured lines.

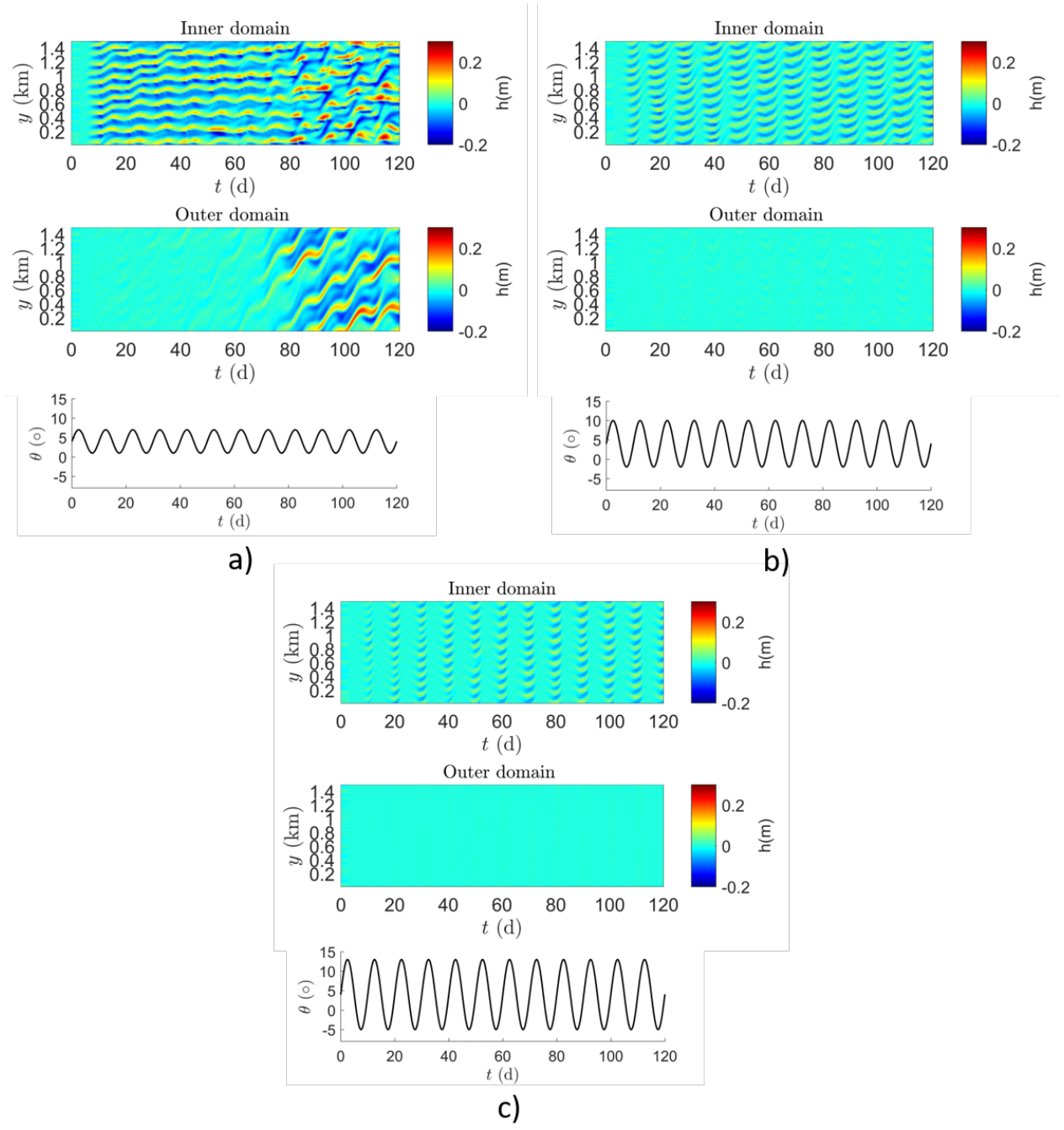

Figure 38: The longshore sections of a) Run6T$_{10}$ ($A_\theta = 3^o$), b) Run7T$_{10}$ ($A_\theta = 6^o$) c) Run8T$_{10}$ ($A_\theta = 9^o$). The longshore direction in km is given on the vertical axis and time t in days is given on the horizontal axis. The perturbations on top of the uniform bars is given by the colours with blue the deepened areas, so erosion takes place, and red areas that became more shallow, so net sedimentation takes place. The angle of incidence in degrees at the offshore boundary as a function of time is also plotted for all cases.

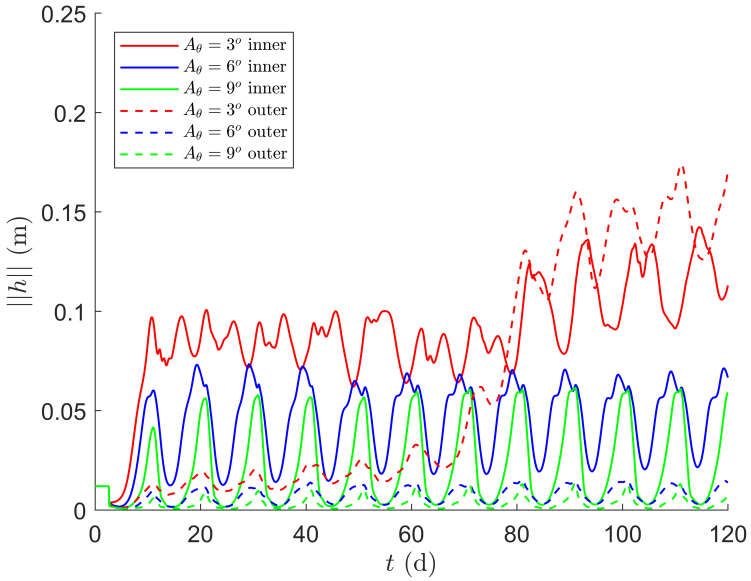

Figure 39: The root-mean square bar height $||h||(t)$ in meters as a function of time in days is given for Run6T$_{10}$, Run7T$_{10}$ and Run8T$_{10}$ as the red line, the blue line and the green line respectively. With the inner domain indicated by the solid line and the outer domain with the dashed line. This shows the influence of the amplitude of the of the wave angle at the offshore boundary at the mean growth rate ate the two domains.

,